

Magic tricycles: efficient magic state generation with finite block-length quantum LDPC codes

Varun Menon^{*†}, J. Pablo Bonilla Ataides^{*}, Rohan Mehta, Daniel Bochen Tan, and Mikhail D. Lukin

Department of Physics, Harvard University, Cambridge, MA 02138, USA

August 15, 2025

Abstract

The preparation of high-fidelity non-Clifford (magic) states is an essential subroutine for universal quantum computation, but imposes substantial space-time overhead. Magic state factories based on high rate and distance quantum low-density parity check (LDPC) codes equipped with transversal non-Clifford gates can potentially reduce these overheads significantly, by circumventing the need for multiple rounds of distillation and producing a large number of magic states in a single code-block. As a step towards realizing efficient, fault-tolerant magic state distillation, we introduce a class of finite block-length quantum LDPC codes which we name tricycle codes, generalizing the well-known bicycle codes to three homological dimensions. These codes can support constant-depth physical circuits that implement logical CCZ gates between three code blocks. We show that these tricycle codes enable magic state generation with single-shot state-preparation and error correction, leading to a deterministic low-overhead distillation protocol without requiring post-selection. Numerical simulations of specific codes confirm robust performance under circuit-level noise with a Belief-Propagation+Order-Statistics Decoder (BPOSD), demonstrating a high circuit-noise threshold of $> 0.4\%$. Finally, we construct optimal depth syndrome extraction circuits for tricycle codes and present a protocol for implementing them efficiently on a reconfigurable neutral atom array platform.

Contents

1	Introduction	2
1.1	Background	2
1.2	Summary of results	4
1.3	Related work	6

^{*}These authors contributed equally to this work.

[†]varunmenon@g.harvard.edu

2 Main results	6
2.1 Tricycle codes	6
2.2 Transversal <i>CCZ</i> circuits	8
2.3 Single-shot distillation	11
2.4 Circuit-noise simulations	14
2.5 Implementation of syndrome extraction circuits	16
3 Discussion and Outlook	17
4 Acknowledgments	19
A Code construction and properties	19
B Cup products and transversal CCZ action	23
C Logical circuit optimization	29
D Determining code distances	30
E Numerical details of noise simulations	32
F Optimal-depth syndrome extraction circuits	32
G Neutral atom array architecture and rearrangement procedure	35
Supplementary Material	46

1 Introduction

1.1 Background

Universal fault-tolerant quantum computation requires the implementation of both Clifford and non-Clifford operations on the logical qubits of a quantum error correcting code [36]. Logical Clifford gates can often be implemented *transversally* in many codes – that is, by a physical circuit with a depth that is constant in the size of the code. Transversal gate architectures are naturally fault tolerant as the spread of errors between physical qubits of the code is inherently bounded. However, a seminal result of Eastin and Knill proves that it is not possible to implement a universal gate set transversally in a quantum error correcting code [29]. Since it is desirable to implement as many gates transversally as possible, many architectures for fault-tolerant quantum computation utilize codes with a transversal Clifford gate set, while non-Clifford gates, also known as *magic gates*, are implemented by teleporting specially prepared non-Clifford resource states into the codespace. One class of protocols for the fault-tolerant preparation of such high-fidelity resource states, known as

magic state distillation (MSD), relies on quantum error correcting codes with a transversal magic gate to refine a large number of noisy input magic states into a smaller number of output states with improved fidelity. To achieve the target output fidelity, typical MSD schemes such as the 15-to-1 distillation (15-1-3) protocol [15] require multiple levels of repeated distillation, as well as concatenation with an inner code of sufficiently large distance that supports transversal Clifford gates, contributing significantly to the space-time overhead of the protocol. As such, in state-of-the-art fault-tolerant architectures, the overhead associated with magic state distillation has been estimated to dominate total qubit and gate counts – for example, magic state generation dominates the latest resource estimates of factoring RSA integers with Shor’s algorithm despite significant optimizations [33, 99].

Over the last decade, remarkable progress has been made towards significantly reducing the overhead associated with magic state distillation by designing various codes with transversal non-Clifford gates and favorable code parameters [14, 50, 40, 21]. In fact, it has very recently been shown that families of quantum codes with transversal non-Clifford gates and asymptotically constant rate and relative distance exist, leading in principle to constant spatial overhead MSD protocols [63, 94]. However, these proposals come with two important caveats. First, the proposed codes in such low-overhead distillation schemes have high-weight parity checks with check weights that are typically extensive in the block length of the code. As such these codes are not obviously fault-tolerant on their own in the presence of circuit-level noise as they require syndrome extraction circuits with depths that grow with the block-length, and thus may not support a finite threshold or exponential sub-threshold error suppression. Moreover, the extensive depth of syndrome extraction circuits of these codes implies that the temporal overhead associated with distillation from these codes is significant. Second, some of these constructions require constant-depth Clifford corrections on top of a transversal non-Clifford circuit to achieve the desired logical action. These schemes implicitly assume that Clifford operations are noiseless – an assumption that is justified when concatenating the distillation code with an inner code that has transversal Clifford operations such as the two-dimensional color code. Practically, the overhead of these protocols is therefore exaggerated by the requirement of a sufficiently high distance inner code so that the distillation protocol is not bottlenecked by the error-rate of Clifford operations.

Quantum low-density parity-check (qLDPC) codes, which simultaneously admit sparse stabilizer checks and favorable rate and distance scaling, have been proposed as a pathway toward reducing the cost of quantum error correction. In the context of quantum memory, qLDPC codes with asymptotically constant rates and relative distances have recently been shown to exist [67, 53], and several architectures for implementing qLDPC memories on superconducting and neutral-atom architectures have been proposed [5, 95, 96, 13]. However, the application of general qLDPC codes to magic state distillation protocols has only recently begun to be explored, in part because of the difficulty of constructing codes that host transversal non-Clifford gates. Utilizing appropriate qLDPC codes could dramatically reduce the overhead of MSD protocols for a number of reasons. Codes with high relative distances ensure effective error suppression during distillation, while high rate codes allow multiple magic states to be distilled in parallel within a single block, improving throughput. In contrast to traditional MSD schemes that rely on small codes concatenated many times, LDPC codes can potentially achieve the same target fidelity in a single round, greatly reducing space-time overhead. While this is also true for the aforementioned non-LDPC constant-overhead and low-overhead MSD protocols, crucially, qLDPC codes enable these properties while maintaining fault-tolerance with constant-depth syndrome extraction circuits. Moreover, for qLDPC codes with

strongly-transversal non-Clifford gates (i.e a constant depth physical circuit of non-Clifford gates without a Clifford correction), there is no need for concatenation with an inner code with transversal Clifford gates. Constructions of practical LDPC magic state factories are thus highly desirable for fault-tolerant quantum computing architectures.

Motivated by these considerations, this work introduces a class of finite block-length, high-rate and distance quantum LDPC codes with a transversal logical CCZ circuit action for magic state distillation, which we call ‘tricycle codes’. These codes are constructed as the three-dimensional *balanced product* [17], a particular generalization of the homological product, of classical binary linear codes over Abelian group algebras [44]. This construction extends the two-block group algebra codes of [49, 54] (also known as bicycle codes [65]) into three dimensions, allowing in principle for transversal gates from the third level of the Clifford hierarchy [37]. We may thus also refer to the tricycle codes as ‘three-block Abelian group-algebra codes’. It is worth highlighting that for the task of magic state distillation, high-rate and high-distance finite block-length codes are sufficient for essentially any large-scale quantum computation. For example, codes with distances large enough to achieve a logical error rate of 10^{-12} at attainable physical error rates are expected to be sufficient to produce magic states to execute large-scale quantum algorithms such as Shor’s algorithm [78] fault-tolerantly. We present several examples of finite block-length codes that achieve low logical error rates under circuit level noise at a physical error rate of 10^{-3} .

The theoretical formalism we utilize for constructing transversal non-Clifford gates in three-dimensional product codes comes from endowing the codes with a *cup product*, an operation from algebraic topology and homological algebra, related to the triple-intersection of logical operators of the code, which we discuss further in Sec. 2.2 and Appendix B. At a high level, this formalism allows general product quantum CSS codes to be equipped with the necessary structure to host transversal gates ascending the Clifford hierarchy. In fact, the transversal non-Clifford gates of three-dimensional color codes can also be interpreted in terms of cup-products on the associated three-dimensional cellular complexes [9]. Recent work by Breuckmann et al. introduced a general formalism to endow the co-chain complexes associated with homological product and balanced product quantum codes with cup-product operations and classified the associated gates they give rise to [16]. In this work, we leverage this formalism for the tricycle codes and study the transversal logical non-Clifford circuits they host in detail. We present several concrete examples of these codes with high rates and distances, study their performance under realistic circuit level noise, and explore their application to practical magic state distillation protocols.

1.2 Summary of results

The tricycle codes we construct achieve favorable parameters at relatively small block lengths. We introduce several codes with check weights $w_x = 12$, $w_z = 8$, where w_x and w_z denote the weights of the X and Z checks of the code respectively. We use the notation $[[N, K, D]]$ to report the block-length N , number of encoded logical qubits K , and minimum distance D of quantum codes. We find codes which encode 15 logical qubits using 375 physical qubits, with parameters $[[375, 15, \leq 15]]$, as well as some $[[405, 9, \leq 20]]$ codes. Smaller codes such as those with parameters $[[192, 27, 8]]$ and $[[72, 9, 6]]$ are also found. The largest code we study in detail is a $[[648, 18, \leq 18]]$ code. A list of several such codes along with their parameters is presented in Table 1.

We show that tricycle codes host constant depth physical circuits that preserve the code-space,

consisting solely of CCZ gates between three code blocks, of depths 4, 8, 12, 16, 18, depending on choices made in the code construction, which in turn also affect the rates and distances of the code. In particular, we show that all tricycle codes host a depth 18 code-space preserving CCZ circuit. Reducing the depth of the CCZ circuit requires additional constraints in the code construction (discussed in Appendix B). The logical action of the CCZ circuits depends on a choice of a representative logical operator basis in each code-block, but is generically a circuit of logical CCZ gates. When such a circuit acts on the $|+, +, +\rangle^{\otimes K}$ logical state of three code-blocks it produces a high magic state known as a *hypergraph* magic state [100, 22]. Such a hypergraph magic state embeds $K_{CCZ} \leq K$ many disjoint $\overline{CCZ} \cdot |+, +, +\rangle$ magic states which can be extracted using gate-teleportation techniques. The physical CCZ circuit, factors determining their depths, and the logical action they induce for particular codes are discussed in Sec. 2.2 and Appendix B.

We further show that the tricycle codes are single-shot [7] in the Z -measurement basis. We show in Sec. 2.3 that this property enables a distillation protocol that requires only a constant number of rounds of syndrome extraction during error correction cycles instead of $O(d)$ rounds, where d is the code distance. Moreover, we present numerical evidence that tricycle codes exhibit the stronger notion of single-shot state-preparation, allowing the initial logical state of a magic state preparation circuit to be prepared in constant depth. To the best of our knowledge, this is the first example of such a single-shot magic state distillation protocol.

We analyze the performance of select tricycle codes under a realistic circuit level noise model in Sec. 2.4 using a belief-propagation decoder with order-statistics post-processing (BPOSD) [72]. By comparing the performance of codes across a range of block-lengths, we are able to ascertain a high-threshold for tricycle codes under circuit-level noise of above 0.4% with BPOSD decoding. We note that although the codes we present are finite-block length codes, the construction allows us to define a family of codes by choosing a single high-performing tricycle code from a given block-length. Although such a code family is unlikely to be asymptotically good, we expect that a larger block-length code with a larger distance can always be found – a claim that is supported by the distance lower bound we prove in Appendix A. Defining a threshold with respect to such a constructed code family allows one to make guarantees of sub-threshold noise suppression by selecting codes of arbitrarily large block-lengths with larger distances. We expect the quoted 0.4% threshold to improve significantly with better decoders, as we find that circuit level performance is highly sensitive to BPOSD hyperparameters.

We also show how to construct compact syndrome extraction circuits of optimal depth (depth 12 excluding state preparation and readout for the $w_x = 12, w_z = 8$ codes we consider). Finally, we present a concrete protocol for efficiently implementing the preparation and syndrome extraction of tricycle codes on a reconfigurable neutral-atom array platform – a video illustrating the atom-moving scheme for syndrome extraction of tricycle codes is provided in the ancillary files that accompany this manuscript.

Our work serves as a step toward a new class of distillation protocols that leverage the structural properties of quantum LDPC codes to reduce resource overhead in universal fault-tolerant computation. Such distillation schemes are naturally suited to fault-tolerant quantum computing architectures that utilize LDPC quantum memories along with universal adapters for magic state injection, such as in Ref. [96, 97]. An important open problem that would make the ideas presented in this work even more efficient is to construct schemes for the efficient extraction of prepared magic states from LDPC factories in parallel, instead of teleporting gates into a computational code one

logical qubit at a time.

1.3 Related work

Several recent works introduce binary quantum LDPC code families with asymptotically high rates and relative distances with transversal logical CCZ action. Golowich and Lin [35] constructed a family of codes based on homological products of classical Sipser-Spielman expander codes [80] with local Reed-Muller codes [69, 62] with near-constant rate and relative distance that supports transversal logical non-Clifford gates. These codes however have check-weights that are not constant but grow logarithmically in the block-length. Lin also introduced a general formalism for constructing LDPC quantum code families with transversal non-Clifford gates based on algebraic sheaves [55]. Similarly, Zhu introduced a family of topological codes with constant rate and polynomial distance with transversal CCZ gates [100, 101]. Quantum rainbow codes were introduced as generalizations of color-codes with transversal non-Clifford gates to higher-dimensional simplicial complexes [77], achieving asymptotically constant rate and logarithmic distance. Finally, Breuckmann et al. [16] discuss how to construct constant rate and polynomial distance families with transversal gates that ascend the Clifford hierarchy using iterated homological and balanced products of chain complexes and the cup-product gate formalism they develop, which we also utilize in this work.

Adding to these remarkable results, this work focuses on a particular class of high-performance finite block-length codes. It is unclear precisely how large the smallest elements of the code families in the aforementioned works are, but constructions based on three-fold homological products of classical codes likely involve at-least several thousand and potentially tens of thousands of physical qubits for the smallest attainable block-lengths with good parameters, due to the cubic growth of the size of the quantum code with respect to the classical codes. The significantly smaller block-lengths of the tricycle codes presented in this work is one of the primary reason we chose to study them. A direct comparison of overhead and performance of the LDPC codes from the above constructions with each other and the tricycle codes we present would be an interesting direction for future work.

2 Main results

2.1 Tricycle codes

Throughout this work, we denote the binary field by $\mathbb{F}_2 \equiv \{0, 1\}$ where arithmetic is modulo 2. The tricycle codes are quantum CSS codes [19, 83] defined by the binary block parity check matrices

$$H_X = [\mathbf{A}^T \quad \mathbf{B}^T \quad \mathbf{C}^T] \in \mathbb{F}_2^{n_G \times 3n_G} \quad H_Z = \begin{bmatrix} \mathbf{C} & \mathbf{0} & \mathbf{A} \\ \mathbf{0} & \mathbf{C} & \mathbf{B} \\ \mathbf{B} & \mathbf{A} & \mathbf{0} \end{bmatrix} \in \mathbb{F}_2^{3n_G \times 3n_G} \quad (1)$$

where $\mathbf{A} = \sum_{i=1}^{w_a} \mathbf{A}_i \in \mathbb{F}_2^{n_G \times n_G}$, $\mathbf{B} = \sum_{i=1}^{w_b} \mathbf{B}_i \in \mathbb{F}_2^{n_G \times n_G}$, $\mathbf{C} = \sum_{i=1}^{w_c} \mathbf{C}_i \in \mathbb{F}_2^{n_G \times n_G}$ for constants w_a, w_b, w_c , and $\mathbf{A}_i, \mathbf{B}_i, \mathbf{C}_i$ are permutation matrices – i.e matrices with a single 1 in every row and column. The parameter n_G is the linear size of each block and is related to the size of a finite group (hence the subscript G) – the details of this connection are discussed in Appendix A. These parity check matrices thus define codes on $N = 3n_G$ qubits. Modulo two arithmetic implies immediately

that the CSS orthogonality condition $H_Z H_X^T = 0$ is satisfied. Moreover, the matrices \mathbf{A} , \mathbf{B} , \mathbf{C} commute pair-wise. There are n_G many X -checks of weight $w_a + w_b + w_c$ and $3n_G$ many Z -checks which can be partitioned into three sets of n_G checks each with weights $w_c + w_a$, $w_c + w_b$, and $w_b + w_a$ respectively. By choosing $w_a = w_b = w_c = w$ for a constant w , these codes are $(w, 3w)$ -regular LDPC codes in the X basis and $(2w, 2w)$ -regular LDPC in the Z basis, where (p, q) -regular means that every qubit is involved in exactly p checks and each check involves exactly q qubits. Examples of particular codes from this construction in Table 1 demonstrate that the checks are typically highly redundant – often leading to favorable code parameters and ease of decoding – since the total number of checks $4n_G \gg N - K = 3n_G - K$. This observation is encapsulated by the fact that tricycle codes possess *meta-checks* in the Z basis – these are relations between the Z checks encoded in a matrix H_{meta} such that $H_{meta} \cdot H_Z = 0$. We discuss the meta-check structure and its implications in Sec. 2.3.

To ensure practical feasibility of implementing these codes in early fault-tolerant architectures below pseudo-threshold error rates, we restrict our attention to codes constructed with $w = 4$, producing codes with a maximum check weight of 12 – in particular, the X -checks have weight 12 while the Z -checks have weight 8. There are two reasons we consider $w = 4$. The first is that the cup-product transversal CCZ gate formalism of Ref. [16] that we use requires w to be even for these codes (details are in Appendix B). The second is that we empirically found that all codes with $w = 2$ had a maximum distance of 6 and relatively poor rates regardless of the code block-length (to the extent of our numerical search).

N	K	D_X	D_Z
72	9	12	6
144	6	≤ 24	10
192	27	16	8
375	15	≤ 25	≤ 15
405	9	30	≤ 15
648	18	≤ 48	≤ 18

Table 1: **Examples of tricycle codes and their parameters for various block-lengths.** N is the block-length, K the number of encoded logical qubits, D_X and D_Z are the minimum weights of logical X -type and Z -type operators respectively. The distances of codes are found exactly by using either a SAT-solver to find the shortest error [32] or a mixed integer program [51] when feasible. Otherwise, distances are estimated – sometimes, with strong statistical guarantees, in which case we report the distance as exact¹ – using the low-weight biased Monte-Carlo sampling method discussed in Appendix D with 100 million shots. The construction of these specific codes is described in Appendix A and Table 4.

The codes in Table 1 have imbalanced distances with $d_Z \leq d_X$. Based on an extensive numerical search over several tens of millions of codes, we conjecture that this is true for all tricycle codes (Conjecture 1 in Appendix A). The imbalanced distances of these codes is a particularly useful feature for experimental platforms which are typically dominated by noise biased towards one basis. A detailed exploration of how noise bias can boost the experimental performance of tricycle codes is left for future work.

Overall, the high distances of tricycle codes combined with the transversal CCZ circuits they

host (which we discuss in Sec. 2.2) make them ideal candidates for magic state factories for various target logical error rates. While the rates of these codes are lower than their two-dimensional counterpart bicycle codes (see the codes in Ref. [13] for example), they are much higher than the rates of three dimensional binary homological product codes of comparable block-length, including the $3D$ color code.

2.2 Transversal CCZ circuits

Tricycle codes support constant-depth, code-space preserving circuits built from physical CCZ gates acting across three code blocks. Each block contains $3n_G$ qubits, partitioned into three equal-size sectors labeled I , II , and III , each with n_G qubits. We label each qubit as q_i^j , where $i \in \{1, 2, 3\}$ denotes the code block and $j \in \{I, II, III\}$ the sector. Within each sector, qubits are indexed arbitrarily but consistently across blocks.

The structure of a transversal CCZ circuit is encoded in a binary function

$$f_{CCZ} : Q \times Q \times Q \rightarrow \mathbb{F}_2, \quad (2)$$

where Q is the set of all physical qubits. A value $f_{CCZ}(q_1^{j_1}, q_2^{j_2}, q_3^{j_3}) = 1$ indicates a physical CCZ gate between the specified qubits, one from each code block. Otherwise, no gate is applied. This is illustrated in Fig. 1a). f_{CCZ} is then linearly extended to be defined as a trilinear function on all computational basis states. To define a valid, code-space preserving circuit, f_{CCZ} must satisfy two additional conditions:

1. f_{CCZ} must vanish when any argument corresponds to a binary string b defining an X -type stabilizer – i.e $X^b = X^{b_1} \otimes X^{b_2} \cdots \otimes X^{b_{3n_G}}$ is an X -type stabilizer. This condition ensures f_{CCZ} descends to a well-defined function on the space of logical codewords.
2. f_{CCZ} must define a constant-depth circuit of physical CCZ gates.

We expand on both conditions and their homological interpretation in Appendix B. See Proposition 2 for how f_{CCZ} is defined for tricycle codes.

Breuckmann et al. [16] introduced a general formalism for constructing appropriate trilinear functions f_{CCZ} that satisfy conditions 1 and 2. Using this framework, we show that all tricycle codes with check-weights $(w_X, w_Z) = (12, 8)$ admit depth-18 transversal CCZ circuits. Shallower circuits – down to depth 4 – can be constructed by imposing additional structure on the code, such as constraints on the matrices $\mathbf{A}, \mathbf{B}, \mathbf{C}$ used to define the parity checks in Eq. (1). Details of these constructions appear in Appendix B, and representative examples are listed in Table 2. While shorter-depth codes tend to have lower distance or rate, we observe that increasing block size recovers performance, suggesting no intrinsic limit on code parameters from enforcing such circuit-depth reducing conditions.

We distinguish two classes of transversal circuits:

¹Specifically, the method we use returns a confidence interval on the distance conditioned on certain assumptions on the distribution of minimum-weight code-words. These assumptions can in turn be hypothesis tested using the empirical distribution of low-weight code-words found from sampling. We report the distance as exact if the confidence is $> 99.9\%$ and if the p -value associated with the hypothesis test is $> 10\%$. Details of the method are in Appendix D

- **Single-sector circuits**, where each CCZ gate acts on one sector per block – e.g., sector I of block 1, II of block 2, and III of block 3 (illustrated in Fig. 1b).
- **Triple-sector circuits**, where all sectors of all blocks participate in a layered CCZ pattern. These are organized into parallelizable layers for constant depth (see Fig. 1c).

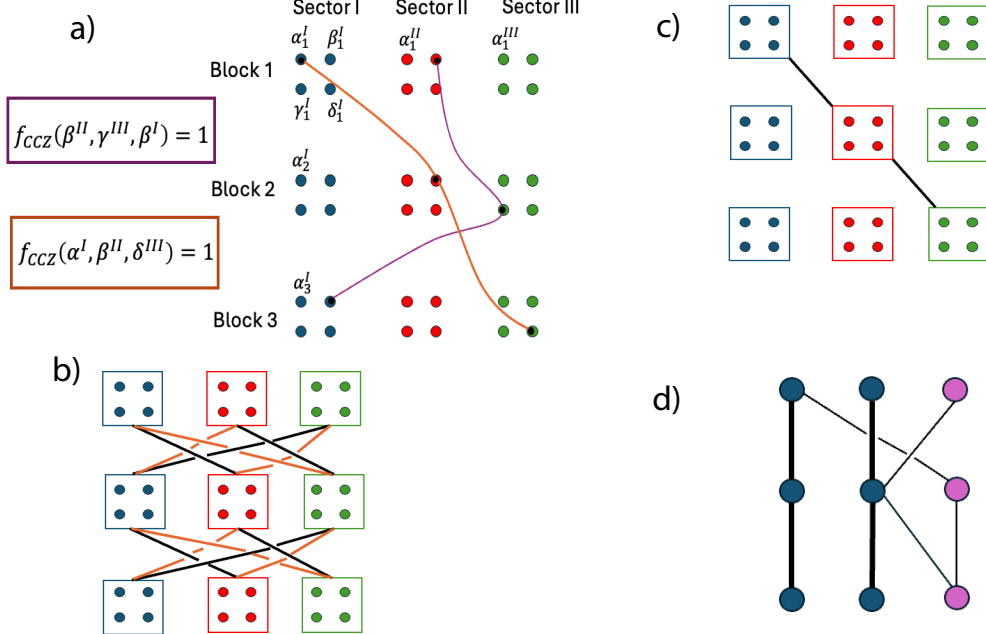


Figure 1: **Structure of transversal CCZ gates of tricycle codes.** a) Schematic of a transversal CCZ circuit on a 12-qubit code. Each code block is partitioned into three sectors of 4 qubits, labeled $\alpha, \beta, \gamma, \delta$ with subscripts and superscripts indicating the code block and sector. Colored curves denote CCZ gates between triples of qubits where f_{CCZ} is non-zero. b) Single-sector CCZ circuit: only one sector per block is active, and each qubit in that sector participates in m CCZ gates for a depth- m circuit. c) Triple-sector CCZ circuit: all sectors participate via two disjoint, parallelizable layers. Each qubit undergoes $m/2$ black and $m/2$ orange CCZ gates, executed in m total depth. d) Logical CCZ connectivity after basis optimization for a $K = 3$ code. Circles denote logical qubits; rows correspond to separate code blocks. Thick black lines indicate usable \overline{CCZ} gates for magic state distillation ($K_{CCZ} = 2$ shown), while thin lines involve gauge qubits (pink), initialized in $|0\rangle$. Blue circles represent logical qubits in disjoint triples connected only to other qubits in the triple or to gauge qubits.

The logical action of a transversal CCZ circuit is derived by restricting f_{CCZ} to the logical subspace, using representatives of logical X operators for each block. This produces logical \overline{CCZ} gates between triples of logical qubits whenever $f_{CCZ}(l_1^i, l_2^j, l_3^k) = 1$, where $\{l_1^i\}_{i=1 \dots k}$ are a representative basis set of logical X operators of the first code-block, with $\{l_2^j\}$ and $\{l_3^k\}$ defined similarly. The resulting state, obtained by applying the logical circuit to $|+, +, +\rangle^{\otimes K}$, defines a *hypergraph magic state* [100, 22], with vertices as logical qubits and hyperedges as \overline{CCZ} gates. Recent work studies such hypergraph magic states, arguing that they can contain a large amount of magic and can be classically hard to simulate [22].

While the produced hypergraph magic states are interesting and potentially computationally useful in their own right, we would also like to be able to extract smaller component magic gates from the logical circuit for quantum computation. One way to achieve this is to demand that the logical circuit consists of $K \overline{CCZ}$ gates across code-blocks, each acting on disjoint triples of logical qubits. However, a choice of logical bases that produces such a logical circuit may not always exist (and is unlikely to). We may instead try to maximize the number of extractable \overline{CCZ} gates on disjoint triples of logical qubits $K_{CCZ} \leq K$. Finding such a subset corresponds to computing the *subrank* of the f_{CCZ} function restricted to logical operators, a known problem in tensor rank theory [24, 48, 35, 55]. We use a mixed-integer programming method to find feasible solutions to this problem (Appendix C), and below we report the best values of K_{CCZ} found for each code in Table 1 and Table 2. For most codes, our solvers eventually time out within computational resource constraints without proving optimality, suggesting that larger K_{CCZ} values than the ones we report are possible to find with tailored heuristic optimization strategies – a promising avenue for future work. The resulting logical circuits enable the extraction of K_{CCZ} usable \overline{CCZ} gates. Logical qubits not used in these gates are treated as *gauge qubits* and initialized in the $|0\rangle$ state, which nullifies any \overline{CCZ} gates they participate in (Fig. 1d) – see Appendix B for details.

Using the methods described in Appendix C, we are able to find at-least $K_{CCZ} \geq 5$ for the $N = 192, 375, 405, 648$ qubit codes and $K_{CCZ} \geq 4$ for the $N = 72, 144$ codes in Table 1 using the depth 18 CCZ circuit – see Appendix B. We attempted to find larger values of K_{CCZ} for these codes, but the solver we used did not converge within a reasonable amount of time. We therefore emphasize that the K_{CCZ} values found here are lower bounds returned by exact methods that quickly become infeasible for larger K_{CCZ} – this is primarily due to the current lack of well-performing efficient heuristics for the binary tensor-subrank problem, and we anticipate that progress towards such heuristics will lead to a higher yield of individually distillable \overline{CCZ} type magic states for the codes in Table 1.

On the other hand, for some of the codes with short-depth CCZ circuits from Table 5, we were able to determine the exact values of K_{CCZ} . For the $N = 135$ codes with depth 4 and depth 8 CCZ circuits from Table 5, we found $K_{CCZ} = 1$ in both cases. For the $N = 405$ depth 4 and depth 8 codes, we similarly found $K_{CCZ} = 3$ in both cases. A more extensive search over tricycle codes with shorter CCZ circuit depths may reveal codes with larger K_{CCZ} – our search over codes with short-depth circuits is far from exhaustive, and we did not select for short-depth codes with large K_{CCZ} in the numerical search, focusing instead on code parameters. However, it remains a possibility that imposing the additional constraints needed to reduce the depth of CCZ circuits (see Appendix B) generically leads to lower attainable K_{CCZ} values – further work is needed to ascertain whether this is the case. For completeness, we note that for the depth 12 and 16 CCZ circuit codes in Table 2, our methods once again returned lower bounds of $K_{CCZ} \geq 4$.

A subtle point that is understated in LDPC magic state distillation proposals is that extracting such K_{CCZ} disjoint \overline{CCZ} gates from the full logical circuit requires the ability to selectively initialize the gauge logical qubits in the $|0\rangle$ state while other logical qubits are initialized in the $|+\rangle$ state. For example, the proposals in Ref. [35, 55, 100, 101, 16] assume the ability to do this. However, selective state initialization is non-trivial for LDPC codes, and in general it is not clear that this is possible in constant depth. Extensions of the techniques introduced in Ref. [96] for initializing arbitrary Pauli product states in homological product codes be useful for selective initialization. We have also become aware of upcoming work [59] that will introduce batched Pauli-product state-

$[[\mathbf{N}, \mathbf{K}, (\mathbf{D}_x, \mathbf{D}_z)]]$	CCZ depth	Circuit type
$[[135, 3, (\leq 22, 8)]]$	4	SS
$[[405, 9, (\leq 27, 10)]]$	4	SS
$[[135, 3, (\leq 27, 9)]]$	8	SS
$[[405, 9, (\leq 29, 11)]]$	8	SS
$[[405, 9, (\leq 37, 14)]]$	12	SS
$[[405, 9, (\leq 27, 11)]]$	12	TS
$[[375, 15, (\leq 15, 10)]]$	16	TS

Table 2: **Examples of codes with code-space preserving CCZ circuits with depths less than 18.** The column labeled ‘Circuit type’ indicates whether the associated circuit is a single-sector (SS) or triple-sector (TS) circuit. See Appendix B and Table 5 for details of how these codes are constructed.

preparation techniques that can achieve selective state-initialization on arbitrary qLDPC codes in constant overhead, as long as many code-blocks are initialized at once in the same state – we anticipate that these techniques will be very useful in a LDPC \overline{CCZ} magic state factory setting. More generally however, we would like to emphasize an alternative perspective of viewing the global hypergraph magic state of the K logical qubits as a high-magic resource state [22], that can be used to perform useful quantum computations in a target computational code with transversal Clifford operations using appropriate circuit compilation techniques. We leave a detailed exploration of this perspective along with concrete protocols for efficient gate-teleportation between tricycle codes and target Clifford gate-set computation codes for future work.

2.3 Single-shot distillation

We now describe how tricycle codes enable single-shot magic state generation. By initializing three code blocks fault-tolerantly in $|\mp\rangle$ using a single round of error correction, and subsequently applying the transversal CCZ circuit described in the previous section, we obtain high-fidelity hypergraph magic states—all within constant circuit depth and without postselection, as illustrated in Fig. 2.

Our approach to constant-depth preparation of logical $|\mp\rangle$ hinges on two essential properties: intrinsic fault tolerance in one stabilizer basis during state initialization, and the presence of metachecks that enable single-shot error correction in the complementary basis. Specifically, we initialize the physical data qubits in the product state $|+\rangle^{\otimes n}$ and perform a single round of stabilizer measurements. As tricycle codes are CSS codes, the X -type checks are implemented as products of physical X operators acting on the input $|+\rangle$ states. This leads to deterministic measurement outcomes. This deterministic behavior makes the X checks robust to measurement errors and allows Z errors to be effectively identified and corrected within a single round.

However, initial Z -type stabilizer measurements produce non-deterministic ± 1 outcomes, which must be reliably fixed to $+1$ on hardware before applying the CCZ gate [5]. In contrast to codes like the surface code, which lack single-shot state preparation, tricycle codes embed a sufficient set of metachecks—additional redundancies that allow a decoder to identify and correct syndrome measurement errors. Metachecks essentially form a separate code that protects the stabilizer syndromes

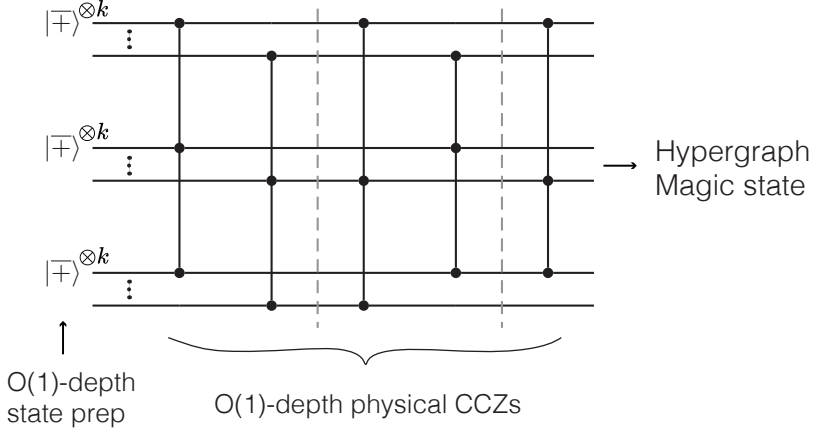


Figure 2: **Single-shot distillation with tricycle codes.** The logical $|\mp\rangle^{\otimes k}$ state of the tricycle code can be prepared fault-tolerantly in constant depth by harnessing the code’s intrinsic resilience in one basis—namely, by preparing the physical qubits such that the associated stabilizer checks are deterministic—together with single-shot error correction in the complementary, non-deterministic, basis. The logical non-Clifford operation is implemented via a constant-depth circuit composed of physical CCZ gates. The output is a logical hypergraph magic state which embeds $K_{CCZ} \leq K$ disjoint logical $|\overline{CCZ}\rangle$ resource states.

themselves. For the Z basis, these take the form

$$H_{meta} = [\mathbf{B} \quad \mathbf{A} \quad \mathbf{C}] \quad (3)$$

where the $\mathbf{A}, \mathbf{B}, \mathbf{C}$ matrices are the same as in Eq. (1). The tolerance to measurement qubit errors is determined by the single-shot distance D_Z^{SS} [20], which is defined as the minimum weight of a faulty syndrome that passes all meta-checks but is not a Z syndrome. A large D_Z^{SS} indicates considerable redundancy, facilitating the identification of sparse syndrome errors. For all codes examined (see Table 1 and Table 2), we find $D_Z^{SS} = D_Z$, or at least share their upper bounds as obtained by Monte Carlo methods (see Appendix D).

In conjunction with *soundness* properties [20] and under select error models, metachecks have been shown to allow for a decoder to fault-tolerantly infer the Z stabilizer eigenvalues after only a constant number of error correction rounds. It is worth noting that this task of preparing the Z stabilizers to $+1$ from a completely random initialization is a more challenging task than just single shot error correction [43, 7], where a decoder may assume that the Z stabilizers were fault-tolerantly fixed to $+1$ prior to the observed noise. For example, many hypergraph product codes enable single-shot error correction but not single-shot state preparation [43].

We supplement our theoretical understanding of the tricycle codes’ single-shot state preparability with a direct simulation of single-shot state preparation for three codes with good finite-size encoding rates and distances. Our results, shown in Fig. 3 demonstrate exponential suppression of the logical error with increased distance, consistent with fault-tolerant state preparation.

Going back to the magic state factory, following initialization, the single-shot error correction capabilities of tricycle codes are paramount to prevent errors from spreading. Each CCZ gate will

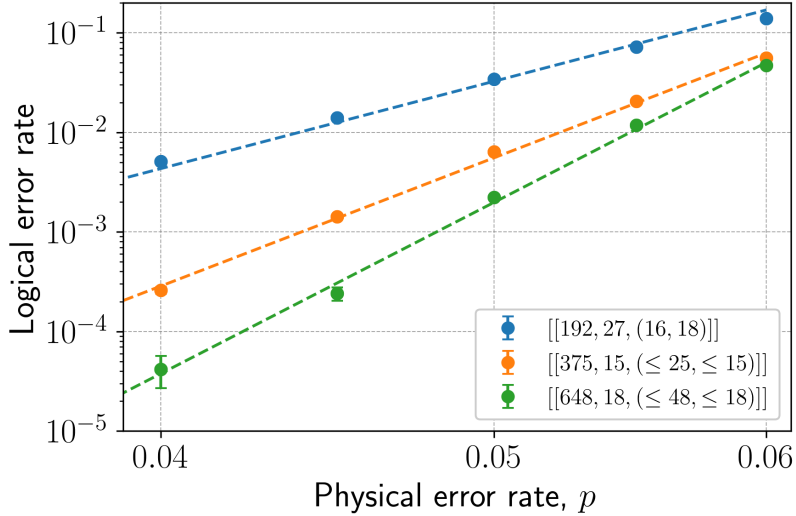


Figure 3: **Phenomenological noise simulation of single-shot state preparation in the Z basis.** Our method resembles Ref. [43] and assumes that the initial Z syndrome is trivial. We apply a round of measurement errors with probability p , followed by two more rounds of syndrome measurement. Pauli X errors occur in each on the data qubits with probability p , in addition to measurement errors. The three rounds of syndrome data are jointly decoded by a BP+OSD decoder [72], corresponding to a three-round windowed decoding protocol (Sec. 2.4). After the inferred correction operator is applied, we perform a noisy transversal Z basis measurement of the data qubits, decode the reconstructed syndrome, and apply the corresponding correction. A logical failure is said to occur if the residual X operator is a logical operator of the tricycle code. Logical error rates are determined via Monte Carlo simulations; error bars indicate standard errors, computed as $\sqrt{p_L(1 - p_L)/M}$, where M is the number of samples.

propagate a pre-existing X error into CZ errors on the other two qubits, which are collapsed into nondeterministic patterns of CZ errors after syndrome measurement. To prevent such errors from building up, the Z stabilizers must continuously be repaired to $+1$. In codes without single-shot properties, this usually requires ‘just-in-time decoding’ [8], in which error clusters are allowed to expand modestly before being corrected, and accompanies a decrease in performance and threshold of the code [75, 76]. The single shot Z basis of the tricycle code, in contrast, is able to immediately correct X errors (up to a small residual error), limiting repeated propagations of CZ errors. Although the X basis is not single-shot, importantly, the Z errors they detect commute with the CCZ gates, so they do not need be corrected in real time. This is opportune given that the CCZ circuit may disrupt the X stabilizer group until the circuit is completed. As the CCZ circuit is of constant depth, it suffices to measure the X stabilizers only after completion; however, incorporating intermediate correction strategies that leverage stabilizer masking [60] could be advantageous.

Together, these results demonstrate that our codes enable fault-tolerant preparation of logical $|\mp\rangle$ states in as little as a single round. As a result, magic state factories based on these codes are extremely compact: the initial state $|\mp\rangle_1 \otimes |\mp\rangle_2 \otimes |\mp\rangle_3$ with all Z stabilizers fault-tolerantly fixed to $+1$ can be prepared in constant depth, and the logical \overline{CCZ} operation can also be implemented in constant depth, as described in the previous section, yielding high-fidelity hypergraph magic states

in constant depth.

We emphasize that these techniques for single-shot distillation are highly unoptimized, and significant improvements in performance are plausible. For instance, post-selecting factory outputs on soft information – the confidence level of the decoder in the produced states’ correctness – is known to considerably decrease the probability of logical failure with only a slight resource overhead [34, 10, 4, 5]. We leave the optimization of this single-shot distillation scheme to future work.

2.4 Circuit-noise simulations

We now evaluate the performance of our codes under realistic circuit-level noise models. Specifically, we demonstrate robust single-shot error correction in the Z basis and assess fault-tolerant behavior in the X basis using repeated rounds of syndrome extraction [13].

To benchmark performance, we simulate errors affecting the entangling gates within the syndrome extraction circuits of tricycle codes, adopting a standard two-qubit depolarizing error model. For a given two-qubit gate error rate p_{2q} , each entangling gate is subject, with equal probability, to one of the fifteen nontrivial two-qubit Pauli errors from IX, IY, \dots, ZZ , and experiences no error with probability $1 - p_{2q}$.

We perform two types of simulations: (1) single-shot simulations in the Z basis, and (2) conventional d -round simulations in the X basis. For the single-shot scenario, we utilize a windowed decoding protocol, wherein each window comprises a fixed number of syndrome extraction rounds followed by decoding and correction. This window is then repeated multiple times, providing a concrete probe of the code’s sustainable logical error suppression [18]. Specifically, our simulations employ windows of three rounds, each repeated fourteen times for a total of forty-two rounds—a protocol previously demonstrated to saturate sustainable performance in high-rate codes [95]. With fixed window size, only codes possessing genuine single-shot capability exhibit logical error suppression that scales with code distance; in contrast, codes lacking such features see their performance limited by the window size. Although a window size of one is theoretically sufficient, empirical studies indicate that size three yields enhanced robustness to measurement errors and generally improved logical error rates [95, 12]. For conventional d -round simulations in the X basis, the syndrome extraction is repeated for d cycles, and decoding is performed using the entire record of accumulated syndrome information.

Decoding is achieved by recasting the syndrome extraction circuits as spacetime codes: checks correspond to parities of stabilizer measurements across consecutive time frames, and qubits are associated with distinct fault locations in the circuit [95, 12]. We employ belief propagation with ordered statistics decoding (BP+OSD) [72] to process the observed syndrome data. In single-shot simulations, belief propagation is applied to each window, except for the final readout which uses BP+OSD; for d -round simulations, BP+OSD is used for decoding the full syndrome record. The d -round simulations are computationally intensive, particularly for larger codes such as the $[[375, 15, \leq 15]]$ and $[[648, 18, \leq 18]]$ instances. Additional details, including decoder parameters and simulation protocols, are provided in Appendix E.

Our simulation results are summarized in Fig. 4. Logical error rate is defined as the probability that any logical qubit within the code block fails under the simulated noise model. We observe a gate-noise threshold greater than 0.4% for each of the X and Z basis results (see the discussion after Theorem A.1 in for further details). By fitting the measured logical error rates to an exponential

decay model, $p_L = \alpha(p/p_{\text{th}})^{\beta n^\gamma}$, we estimate the achievable error rates for both X and Z bases. Table 3 presents logical error rates for two key physical error benchmarks: $p_{2q} = 10^{-3}$, representative of near-term hardware, and 10^{-4} , representative of projected advances, together with relevant code parameters.

We observe robust single-shot performance across several tricycle code instances. d -round performance is weaker, reflecting the higher check weight and reduced distance in the X basis.

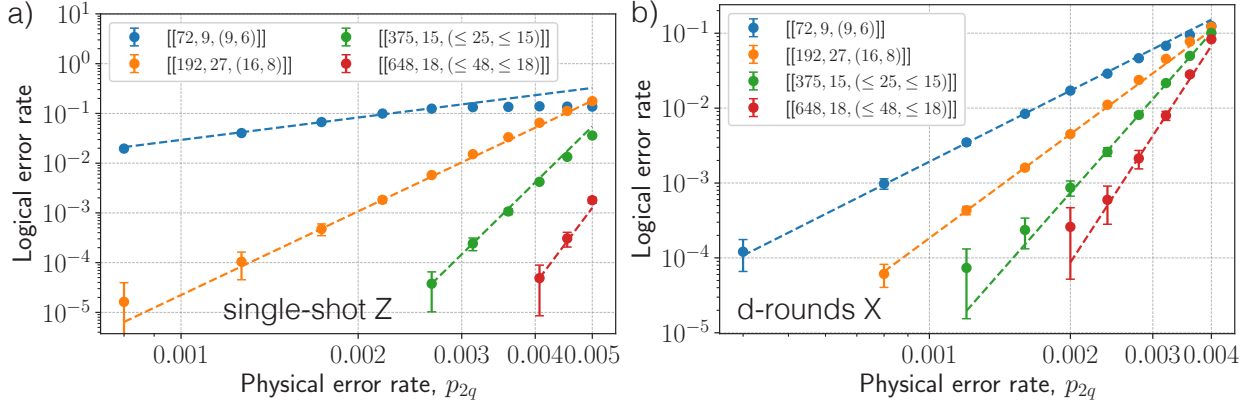


Figure 4: **Circuit-level noise simulation results for tricycle codes.** (a) Logical error rate (as measured by block failure probability) versus two-qubit physical gate error rate (p_{2q}) for single-shot error correction in the Z basis. Single-shot performance is evaluated using a windowed decoding protocol: three rounds of syndrome extraction followed by decoding and correction, with the window repeated 14 times (for 42 total rounds) to probe sustainable suppression of logical errors. (b) Logical error rate versus p_{2q} for fault-tolerant, d -round error correction in the X basis. In both panels, errors are sampled under a standard two-qubit depolarizing circuit-level noise model, and results are shown for various tricycle code. Logical error rates are determined via Monte Carlo simulations using a BP+OSD decoder, with each data point corresponding to M samples; error bars indicate standard errors, computed as $\sqrt{p_L(1 - p_L)/M}$.

$[[N, K, (D_X, D_Z)]]$	$p_L^{(X)}(0.1\%)$	$p_L^{(Z)}(0.1\%)$	$p_L^{(X)}(0.01\%)$	$p_L^{(Z)}(0.01\%)$
$[[72, 9, (9, 6)]]$	2×10^{-3}	3×10^{-2}	1×10^{-6}	9×10^{-4}
$[[192, 27, (16, 8)]]$	2×10^{-4}	2×10^{-5}	4×10^{-9}	6×10^{-11}
$[[375, 15, (\leq 25, \leq 15)]]$	5×10^{-6}	4×10^{-10}	4×10^{-13}	1×10^{-21}
$[[648, 18, (\leq 48, \leq 18)]]$	1×10^{-7}	1×10^{-14}	3×10^{-17}	2×10^{-30}

Table 3: **Example tricycle codes and their simulated logical error rates under circuit-level noise.** Logical error rates $p_L^{(X)}$ and $p_L^{(Z)}$ are shown for both $p_{2q} = 10^{-3}$ and $p_{2q} = 10^{-4}$, for different $[[N, K, D]]$ code parameters.

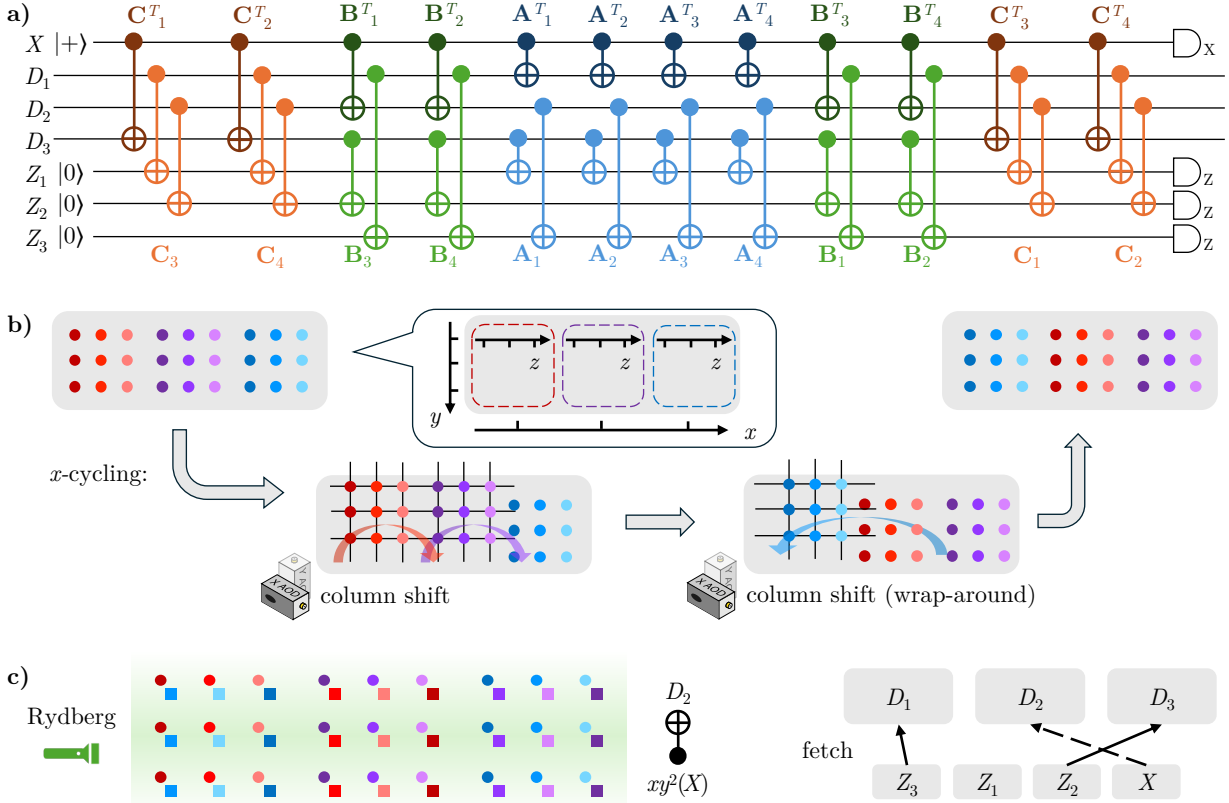


Figure 5: **Implementation of tricycle codes on neutral atom arrays.** (a) Syndrome extraction circuit. Each line denotes a sector. CNOTs are applied on pairs of qubits across two sectors, with the pairing determined by the permutation matrices. (b) Within each sector, physical qubits sharing the same x index form tiles arranged in a row; within each tile, qubits are ordered by their y and z indices. Two AOD movements can realize x -, y -, or z -cycling. (c) Parallel CNOTs can be performed by Rydberg interaction on two overlaying sectors. Data sectors reside in the entangling zone and have larger spacing to avoid intra-sector interactions. After permutation in the workspace below, check sectors are fetched to overlap with the corresponding data sectors and perform CNOTs. Then, check sectors are put back to their original positions, and perform permutation for the next layer.

2.5 Implementation of syndrome extraction circuits

We construct optimal-depth syndrome extraction circuits for the tricycle codes presented. Denote the data qubit sectors as D_1 , D_2 , D_3 , the Z-check sectors as Z_1 , Z_2 , Z_3 , and the X-check sector as X . Our construction is displayed in Fig. 5a, where each CNOT symbol represents a parallel group of physical CNOTs between a check sector and a data sector, associated to a specific permutation. For example, the first CNOT symbol corresponds to CNOTs from the i -th X-check to the j -th qubit in D_3 whenever the (i, j) entry of \mathbf{C}_1^T is 1. Since \mathbf{C}_1^T is a permutation matrix, there is one and only one j for each i . The circuit achieves the optimal CNOT depth of 12. For a proof of correctness and applications of this construction in other settings, see Appendix F.

The syndrome extraction circuit can be implemented on either fixed architectures with all re-

quired couplings fabricated [92], or on reconfigurable architectures with physical qubit permutation [6, 31, 4, 73, 5, 23, 74, 61, 58, 39, 3, 70]. Here, we focus on reconfigurable neutral atom arrays.

With slight abuse of notation, we label the qubits in each sector by indices (x, y, z) , where $1 \leq x \leq n_x$, $1 \leq y \leq n_y$, $1 \leq z \leq n_z$, and $n_G = n_x n_y n_z$. As shown in the callout of Fig. 5b, we place qubits with the same x as tiles arranged in a row; within each tile, qubits are ordered by y and z . Qubits are held in place by traps generated by a spatial-light modulator (SLM); we assume a sufficient number of SLM traps, and thus do not depict them explicitly. Crossed 1D acousto-optic deflectors (AODs) create a 2D grid of mobile traps, enabling entire grids of qubits to be picked up and rearranged in the plane. Our qubit layout leads to efficient implementation of permutation matrices of interest. For example, Fig. 5b illustrates the process of x -cycling, corresponding to cyclically shifting the tiles: first, two tiles are transferred from the SLM to the AOD, shifted right in parallel, and deposited into ancillary SLM traps; the second step applies a ‘wrap-around’ in the opposite direction for the remaining tile. Rows and columns in the AOD grid can otherwise move freely, though their order must be preserved, so the two steps for x -cycling cannot be combined. The y -cycling and z -cycling similarly correspond to cyclically shifting rows and columns within each tile, respectively, as needed to implement polynomial terms like \mathbf{C}_1^T .

Entangling gates are performed by exciting adjacent pairs of qubits to Rydberg states. Parallel CNOTs between corresponding qubits in two sectors are realized by overlaying those sectors and applying a global Rydberg laser pulse, as shown in Fig. 5c (dots and squares denote data and check qubits, respectively. As the colors suggest, the check sector has been permuted with x -cycling by one unit and y -cycling by two units.) To prevent unintended interactions between qubits within the same sector, the pairs are separated by a sufficient distances determined by atom species and Rydberg state.

The overall layout (Fig. 5c, right) places data sectors in SLM traps within the entangling zone. For each CNOT layer, check sectors are permuted in a workspace below and fetched to the corresponding data sectors for parallel CNOTs. In the workspace, smaller grid spacing is used to reduce travel distances for permutation; during fetching, check sectors are expanded to align with data sector spacing. After entanglement, check sectors return to the workspace for the next permutation. Due to crossing movement paths, fetching and put-back of Z-check and X-check sectors must be performed separately in this example to preserve AOD column order.

Executing one syndrome cycle requires a constant number of AOD movements. Let t_{wsp} and t_{ent} denote the time for AOD to traverse a sector in the workspace and the entangling zone, respectively. In the implementation above, permutation, fetch, and put-back for all Z sectors can be done in parallel. Each CNOT layer then involves two fetch and two put-back operations, each bounded by $3t_{\text{ent}}$ (say, from X to D_1). Permutations for Z and X sectors may require x -, y -, and z -cycling, each up to $2t_{\text{wsp}}$. Thus, the per-layer duration is bounded by $12(t_{\text{wsp}} + t_{\text{ent}})$. Further details and possible optimization are discussed in Appendix G.

3 Discussion and Outlook

We have introduced a class of quantum LDPC codes—*tricycle codes*—that support constant-depth, single-shot preparation of logical magic states and show strong resilience to realistic circuit-level

noise. We showed that these codes allow compact, constant depth preparation of high-magic states known as hypergraph magic states while maintaining competitive circuit-level noise suppression and a high threshold of $> 0.4\%$. These hypermagic states in turn embed individually distillable \overline{CCZ} -type magic states, enabling universal quantum computation by using tricycle codes as magic state factories. The promising performance of these codes can be improved further along several directions. The asymmetry between the X and Z sectors of tricycle codes make them particularly advantageous for leveraging noise bias in entangling gate operations—a feature pervasive in leading experimental platforms [1, 5, 64, 79, 11]. Additionally, loss and leakage errors—prevalent in many hardware architectures—represent another avenue for enhancing performance; recent work has shown that appropriate handling of such errors can be leveraged to further improve logical error rates [2, 5]. While our present analysis focuses on unbiased depolarizing noise and neglects loss errors, future studies integrating tailored noise bias exploitation and explicit loss-/leakage-leveraging strategies with these codes are likely to yield further gains and represent a compelling direction for subsequent research.

Beyond their standalone utility as distillation factories, integrating tricycle codes into broader quantum architectures presents several important challenges. A key open problem is the seamless injection or teleportation of distilled magic states into computational code blocks, such as those based on high-performance bicycle codes. While lattice surgery offers a robust, code-agnostic method for logical state transfer—and has seen significant theoretical and experimental development [25, 95, 93, 45, 85, 27, 26]—a particularly promising alternative is transversal teleportation based on natural isomorphisms between tricycle and bicycle codes. Similar to teleportation protocols between 3D and 2D color codes [84, 28], such schemes using transversal one-way CNOT gates between 3D and 2D product codes [42] may enable direct, fault-tolerant transfer of magic states. In particular, we believe this should be possible between bivariate-bicycle codes and bivariate-tricycle codes or between trivariate-bicycle codes and trivariate-tricycle codes, as they share the same product structure. Using extensions of the analytical tools in Ref. [30], we believe it should be possible to show that the logical operators of pairs of some such 2D and 3D group-algebra codes split into isomorphic sectors as in hypergraph product codes [90] – a natural setting for efficient gate teleportation with transversal one-way CNOTs. If realized, these protocols could further reduce space-time overhead and enable highly modular architectures with efficiently integrated magic state distillation.

While we employed the cup-product-gate based construction of Ref. [16] to construct transversal CCZ circuits, alternative approaches may yield shorter-depth circuits or simpler logical structure. Another important direction is improving the yield of disjoint \overline{CCZ} gates that can be extracted from the hypergraph magic states produced by these circuits (Appendix C). This corresponds to the problem of finding the subrank of a binary tensor [24, 48, 35, 55], which is computationally hard. While we used mixed-integer programming, new heuristic strategies could uncover larger values of K_{CCZ} for the codes we consider. In parallel, a deeper understanding of the structure of these high-magic hypergraph states—produced by the transversal CCZ circuits described in Sec. 2.2—may allow one to compile them directly into useful quantum circuits, offering an alternative to extracting only disjoint \overline{CCZ} gates.

In summary, tricycle codes represent a significant step toward scalable, low-overhead, fault-tolerant magic state distillation with quantum LDPC codes. Ongoing work on new code constructions, transversal gate optimization, and efficient code-switching protocols will continue to strengthen the outlook for practical, high-performance quantum computing.

4 Acknowledgments

We thank Nazli Ugur Koyluoglu, Andi Gu, Rohith Sajith, Nishad Maskara, Shayan Majidy, Hengyun Zhou, Harry Putterman, Qian Xu, Brenden Roberts, Jin Ming Koh, Andrei Diaconu, and Prof. Jason Cong for valuable discussions. We acknowledge financial support from IARPA and the Army Research Office, under the Entangled Logical Qubits program (Cooperative Agreement Number W911NF-23-2-0219), the DARPA MeasQuIT program (grant number HR0011-24-9-0359), the Center for Ultracold Atoms (a NSF Physics Frontiers Center, PHY-1734011), the National Science Foundation (grant numbers PHY-2012023 and CCF-2313084), the Wellcome Leap Quantum for Bio program, Harvard Quantum Initiative Postdoctoral Fellowship (DBT) and QuEra Computing. After the completion of this project, we became aware of related work studying tricycle codes, albeit with less focus on transversal magic gates [47].

Appendix

A Code construction and properties

We describe the construction of the tricycle code parity check matrices in more detail, along with general properties of the codes and their connection to balanced products of classical group algebra codes.

Let G be a finite Abelian group, expressed as $G = \mathbb{Z}_{m_1} \times \mathbb{Z}_{m_2} \times \cdots \times \mathbb{Z}_{m_k}$ for some finite k . Let $n_G = |G| = \prod_{i=1}^k m_i$. The codes we construct are defined via matrices over the ring $R := \mathbb{F}_2[G]$, the group algebra of G over \mathbb{F}_2 . Elements of $\mathbb{F}_2[G]$ are formal sums

$$\sum_{g \in G} a_g g, \quad \text{where } a_g \in \mathbb{F}_2,$$

with componentwise addition and multiplication induced by extending the group operation bilinearly. Since G is Abelian, $\mathbb{F}_2[G]$ is a commutative, associative algebra over \mathbb{F}_2 with identity $1_G \in G$.

For $a \in \mathbb{F}_2[G]$, we define its *weight* as $|a| = |\{g \in G \mid a_g = 1\}|$. Each $a \in \mathbb{F}_2[G]$ determines a binary matrix $\mathbf{A} \in \mathbb{F}_2^{n_G \times n_G}$ via

$$\mathbf{A}_{\alpha, \beta} = \mathbb{B}_G(a) \equiv \sum_{g \in G} a_g \delta_{\alpha, g\beta}, \quad (4)$$

where $\alpha, \beta \in G$ and δ is the indicator for $\alpha = g\beta$. The map $\mathbb{B}_G : \mathbb{F}_2[G] \rightarrow \mathbb{F}_2^{n_G \times n_G}$ gives the regular representation of a , following [67].

Alternatively, elements of $\mathbb{F}_2[G]$ can be identified with polynomials via the isomorphism

$$\mathbb{F}_2[G] \cong \mathbb{F}_2[x_1, \dots, x_k]/\langle x_1^{m_1} - 1, \dots, x_k^{m_k} - 1 \rangle, \quad (5)$$

where x_i corresponds to a generator of \mathbb{Z}_{m_i} . Under this identification, the weight of a is the number of monomials with nonzero coefficient in the corresponding polynomial.

To compute \mathbf{A} , let S_l denote the $l \times l$ binary right cyclic shift matrix, and define $\hat{S}_{m_i} = I_{m_1} \otimes \cdots \otimes S_{m_i} \otimes \cdots \otimes I_{m_k}$. These matrices commute for different i . Given $p_a(x_1, \dots, x_k)$, the polynomial

corresponding to a , the binary matrix representation is

$$\mathbf{A} = p_a(\hat{S}_{m_1}, \hat{S}_{m_2}, \dots, \hat{S}_{m_k}). \quad (6)$$

If $|a| = w$, then each row and column of \mathbf{A} has Hamming weight w . We can define tricycle codes formally as follows.

Definition 1 (Tricycle codes). *A three-block Abelian group algebra code (tricycle code) is a CSS code defined by elements $a, b, c \in \mathbb{F}_2[G]$ with weights w_a, w_b, w_c , and binary matrix representations $\mathbf{A}, \mathbf{B}, \mathbf{C} \in \mathbb{F}_2^{n_G \times n_G}$. The X and Z parity check matrices are defined as in Eq. (1), with component matrices formed from binarizing group algebra sums: for example, if $a = a_1 + a_2 + a_3 + a_4$, where $a_i \in G$, then $\mathbf{A} = \sum_i \mathbb{B}(a_i)$.*

We focus on codes with G equal to a product of one, two, or three cyclic groups ($k = 1, 2, 3$). By analogy to the nomenclature for bicycle codes [49, 13, 65], these may be referred to as generalized tricycle, bivariate-tricycle, or trivariate-tricycle codes. We denote the generators by monomials $x_1 \equiv x$, $x_2 \equiv y$, and $x_3 \equiv z$. The polynomials and groups used in the examples of Table 1 are listed in Table 4.

$[[\mathbf{N}, \mathbf{K}, (\mathbf{D}_X, \mathbf{D}_Z)]]$	(l, m, n)	\mathbf{a}	\mathbf{b}	\mathbf{c}
$[[72, 6, (12, 6)]]$	$(2, 3, 4)$	$yz^2 + xz + xyz^2 + xy^2z$	$y + xz + yz^2 + xyz^3$	$y + yz^3 + xyz^2 + xy^2z$
$[[144, 6, (\leq 24, 10)]]$	$(6, 8, \underline{})$	$y^7 + xy^3 + x^4y^5 + x^5y^6$	$x^5 + xy + x^2y^6 + x^4y^2$	$1 + x^3y^7 + x^4y^2 + x^5y^2$
$[[192, 27, (16, 8)]]$	$(4, 4, 4)$	$x^2 + x^3 + y^3 + z^3$	$x^3 + y^2 + y^3 + z$	$x + y^3 + z + z^2$
$[[375, 15, (\leq 25, \leq 15)]]$	$(5, 5, 5)$	$y^4 + z + z^3 + z^5$	$x^2 + x^3 + x^5 + z$	$x^2 + x^3 + z + z^3$
$[[405, 9, (\leq 30, \leq 15)]]$	$(3, 5, 9)$	$x^2 + y + y^2 + z$	$x + y^3 + z^2 + z^3$	$x + y + y^4 + z^5$
$[[648, 18, (\leq 26, \leq 18)]]$	$(6, 6, 6)$	$x^4 + y + z + z^3$	$x + y + y^2 + z$	$x^2 + x^3 + y^4 + z^5$

Table 4: Polynomials used to construct codes in Table 1 corresponding to elements of the group algebra of $G = \mathbb{Z}_l \times \mathbb{Z}_m \times \mathbb{Z}_n$. If there are fewer than three cyclic group factors, the corresponding element in the tuple of group orders (l, m, n) is left empty.

Next, we describe how tricycle codes can be viewed as three-dimensional hypergraph products (HGPs) [90] over non-binary rings, and derive a conditional distance lower bound. We will first need the following definitions.

Definition 2 (Support and intersection subgroups). *Let G be a finite Abelian group, and $a = \sum_{g \in G} a_g g \in \mathbb{F}_2[G]$ with $a_g \in \{0, 1\}$. Define the support subgroup $G_a := \langle \{g : a_g \neq 0\} \rangle$. For elements $a_1, \dots, a_k \in \mathbb{F}_2[G]$, the intersection subgroup is $N = \bigcap_{i=1}^k G_{a_i}$. Since G is Abelian, N is normal in each G_{a_i} .*

Definition 3 (Connected codes). *Let $a, b, c \in \mathbb{F}_2[G]$ with support subgroups G_a, G_b, G_c . The code defined by a, b, c is connected if $G_a G_b G_c = G$. Otherwise, the code decomposes into subcodes supported on cosets of the subgroup $G_a G_b G_c \subset G$, which has order $|G_a||G_b||G_c|/|N|^2$, where N is the intersection subgroup.*

This notion of connectivity extends the Abelian case of [54], which showed that connected two-block group algebra codes can be written as hypergraph products (HGP) over non-binary rings. The same argument applies here, yielding the following:

Proposition 1 (Non-binary 3D HGP). *Let $a, b, c \in \mathbb{F}_2[G]$ define a connected tricycle code, and let $N = G_a \cap G_b \cap G_c$ with $|N| = c$. Let $l_a = [G_a : N]$ be the index of G_a in N , and define l_b, l_c analogously. Define $R = \mathbb{F}_2[N]$, and consider R -valued matrices:*

$$A = A_1 \otimes I_{l_b} \otimes I_{l_c}, \quad (7)$$

$$B = I_{l_a} \otimes B_1 \otimes I_{l_c}, \quad (8)$$

$$C = I_{l_a} \otimes I_{l_b} \otimes C_1, \quad (9)$$

for appropriately chosen $A_1 \in R^{l_a \times l_a}$, $B_1 \in R^{l_b \times l_b}$, and $C_1 \in R^{l_c \times l_c}$. The binary matrices $\mathbf{A}, \mathbf{B}, \mathbf{C}$ are then obtained by applying \mathbb{B}_N element-wise: $\mathbf{A}_{i,j} = \mathbb{B}_N(A_{i,j}) \in \mathbb{F}_2^{c \times c}$, etc.

The parity check matrices correspond to a three-fold R -linear homological product code [98]:

$$H_X^T = \begin{bmatrix} A_1 \otimes I_{l_b} \otimes I_{l_c} \\ I_{l_a} \otimes B_1 \otimes I_{l_c} \\ I_{l_a} \otimes I_{l_b} \otimes C_1 \end{bmatrix}, \quad (10)$$

$$H_Z = \begin{bmatrix} I_{l_a} \otimes I_{l_b} \otimes C_1 & \mathbf{0} & A_1 \otimes I_{l_b} \otimes I_{l_c} \\ \mathbf{0} & I_{l_a} \otimes I_{l_b} \otimes C_1 & I_{l_a} \otimes B_1 \otimes I_{l_c} \\ I_{l_a} \otimes B_1 \otimes I_{l_c} & A_1 \otimes I_{l_b} \otimes I_{l_c} & \mathbf{0} \end{bmatrix}. \quad (11)$$

The binary versions are recovered via the binarization map \mathbb{B}_N defined in Eq. (4).

Proof. This follows identically from the proofs of Statements 7,8,9 in the appendix of [54]. In particular, by choosing a representative set of coset elements $p_i \in G_a/N$, $q_j \in G_b/N$, $r_k \in G_c/N$ where $i = 1 \cdots l_a$, $j = 1 \cdots l_b$, $k = 1 \cdots l_c$, the R -valued matrices A_1, B_1, C_1 are given by

$$(A_1)_{i_1, i_2} = \sum_{n \in N} a_{(p_{i_1} n p_{i_2}^{-1})} n \quad (12)$$

$$(B_1)_{j_1, j_2} = \sum_{n \in N} b_{(q_{j_1} n q_{j_2}^{-1})} n \quad (13)$$

$$(C_1)_{k_1, k_2} = \sum_{n \in N} c_{(r_{k_1} n r_{k_2}^{-1})} n \quad (14)$$

where a_g, b_g, c_g are the coefficients in the group algebra elements $a = \sum_{g \in G} a_g g$ and similarly for b, c . \square

This perspective of viewing connected tricycle codes as three-dimensional homological products over a ring is useful for proving the following lower bound on the code distances.

Theorem A.1. *Consider a connected three-block Abelian group algebra code constructed from group algebra elements $a, b, c \in \mathbb{F}_2[G]$, with corresponding binary matrices $\mathbf{A}, \mathbf{B}, \mathbf{C} \in \mathbb{F}_2^{n \times n}$ where $n = |G|$. Further suppose that the classical binary linear codes with parity check matrices $\mathbf{A}^T, \mathbf{B}^T, \mathbf{C}^T$ have minimum distances d_A^T, d_B^T, d_C^T . We use the convention that $d = \infty$ if the corresponding matrix is full rank. Let $N = G_a \cap G_b \cap G_c$ be the intersection subgroup as defined in Definition 2. The minimum Z distance of the quantum code is bounded below as*

$$d_Z \geq \frac{1}{|N|} \min(d_A^T, d_B^T, d_C^T) \quad (15)$$

Proof. This follows from the proof of Statement 10 in [54]. In particular, Lemma 3 of [54] also holds for three-dimensional homological products by decomposing them into a direct sum of three-dimensional homological products over cyclic group algebras (analogous to Appendix B. in [66]). The matrices $\mathbf{A}, \mathbf{B}, \mathbf{C}$ are constructed identically, and following the proof of Lemma 3. in [54], each component code over a cyclic group algebra can be shown to have all-unit Smith Normal Forms under the assumptions of the lemma. The rest of the proof is identical, applied instead to the matrix H_X defined in Eq. (1). \square

For disconnected codes formed from m connected subcodes, the bound applies to each component and can be summed. In practice, this lower bound is often loose: the codes we construct typically exceed it by a large margin. It may be possible to improve this bound using techniques from [98] adapted to non-binary rings.

While the above bound may not be tight, it does imply the existence of a threshold for tricycle codes. This is because classical quasi-Abelian group-algebra codes with parity check matrices of the form $\mathbf{A}^T, \mathbf{B}^T, \mathbf{C}^T$ are known to include codes that have distances that grow linearly in the block-length [54]. Combined with the above bound, this implies the existence of tricycle codes with distances that are extensive in the block-length with at-least $\sqrt[3]{N}$ scaling, implying the existence of a threshold.

In the following conjecture, we argue that $d_Z \leq d_X$ for the tricycle codes. This would make Theorem A.1 a lower bound on both the X and Z . Although we are unable to construct a formal proof, extensive numerical searches over several millions of random codes indeed validate this claim.

Conjecture 1. *All three-block Abelian group algebra codes defined by Eq. (1) satisfy $d_Z \leq d_X$.*

Next, we explain how tricycle codes arise as the *balanced product* of classical group-algebra codes. This construction builds on the homological formulation of CSS codes and the balanced product construction from Refs. [17, 67, 66, 16], which we assume readers are familiar with in the following discussion – a review is provided in the supplementary material.

A classical group-algebra code is defined by an element $a \in \mathbb{F}_2[G]$, with parity check matrix $H = \mathbb{B}_G(a)$, where \mathbb{B}_G is the binarization map from Eq. (4). This corresponds to the 2-term cochain complex

$$\mathbb{F}_2[G] \xrightarrow{a} \mathbb{F}_2[G] \quad (16)$$

where the coboundary map is given by multiplication by a in the algebra. The bits of the classical code are associated with the 1-cochains (right) and the checks are associated with the 0-cochains (left).

Given two such complexes defined by elements $a, b \in \mathbb{F}_2[G]$, their balanced product results in the 3-term complex

$$R \xrightarrow{\begin{pmatrix} a \\ b \end{pmatrix}} R^2 \xrightarrow{\begin{pmatrix} b & a \end{pmatrix}} R \quad (17)$$

where $R = \mathbb{F}_2[G]$ for notational convenience. Binarizing this complex yields the Abelian bicycle code, with $H_X^T = [\mathbb{B}(a)^T \ \mathbb{B}(b)^T]$ and $H_Z = [\mathbb{B}(b) \ \mathbb{B}(a)]$ [54, 49], where the 0-cochains are X -checks, 1-cochains are qubits, and 2-cochains are Z -checks (with 0,1,2 annotating the spaces in the complex from left to right). This complex arises naturally from the balanced product using the isomorphism $R \otimes_R R \cong R$; see [30, 17, 67] and the supplementary material.

Tricycle codes generalize this by iterating the balanced product once again with a third classical group-algebra code defined by $c \in \mathbb{F}_2[G]$, giving the 4-term cochain complex:

$$R \xrightarrow{\begin{pmatrix} a \\ b \\ c \end{pmatrix}} R^3 \xrightarrow{\begin{pmatrix} c & 0 & a \\ 0 & c & b \\ b & a & 0 \end{pmatrix}} R^3 \xrightarrow{\begin{pmatrix} b & a \end{pmatrix}} R \quad (18)$$

This again follows from expanding the terms of the balanced product complex and applying $R \otimes_R R \cong R$.

The quantum CSS code associated with the tricycle construction is defined by the first three terms of Eq. (18), with consecutive spaces representing X -checks, qubits, and Z -checks respectively. Binarizing the coboundary maps yields the parity check matrices in Eq. (1), and the final map defines the meta-checks in Eq. (3). This complex appears in the appendix of [30], and tricycle codes of this form are also briefly noted in [16].

This homological viewpoint is especially useful for constructing transversal logical gates. In the next section, we apply the formalism of [16] to equip the complex Eq. (18) with an algebraic structure that enables transversal CCZ circuits.

B Cup products and transversal CCZ action

Now we discuss how we derive the transversal CCZ circuits discussed in Sec. 2.2 from the cup-product logical gate formalism of [16].

First, we introduce the necessary formalism at a high level. A cup-product is an algebraic structure that can be defined on some cochain complexes, such as the one in Eq. (18). Let us label the cochain spaces of the complex in Eq. (18) as 0, 1, 2, 3-cochains from left to right, indicated with the notation C^0, C^1, C^2 , and C^3 respectively. Furthermore, we are interested in the case where the C^i are finite-dimensional vector spaces over \mathbb{F}_2 with bases X^i . We define the weight $|c|$ of a cochain $c \in C^i$ as the number of non-zero terms in its basis expansion over X^i . For example, for the tricycle code complex in Eq. (18), the bases X^i are defined by G , and the cochain weight coincides with the weight of group-algebra elements. We will always associate qubits with the 1-cochains of a complex, with 0- and 2-cochains corresponding to spaces of X and Z checks respectively. Thus, we will label the elements of the basis of 1-cochains X^1 by qubit labels $q_1 \dots q_N$ for the N qubits of a CSS quantum code.

A cup-product is then an associative, bilinear map

$$\cup : C^i \times C^j \rightarrow C^{i+j} \quad (19)$$

with the convention that $C^{i+j} = 0$ if $i + j > 3$ in the case of the tricycle complex. Not every such associative bilinear map defines a cup-product; the map \cup must satisfy an additional technical condition known as a Leibniz rule – see [41, 16, 100]. However, given such a cup-product, we can construct a circuit of diagonal physical gates that preserves the code-space of the CSS code associated with the cochain complex. In general, a cup-product on an m -term cochain complex will yield a physical circuit of diagonal $C^{m-2}Z$ gates from the $m-1$ -th level of the Clifford hierarchy [16]. In the situation of interest, we have the 4-term cochain complex in Eq. (18), leading to a circuit of CCZ gates. As discussed in Sec. 2.2, such a circuit can be specified by a trilinear function f

acting on the space of physical qubits – the 1-cochains C^1 in our convention. The circuit associated with the cup-product is then defined by the function

$$f_{\cup}(q_i, q_j, q_k) = |q_i \cup q_j \cup q_k| \in \mathbb{F}_2 \quad (20)$$

where non-zero values indicate a physical CCZ gate acting between the qubits of three distinct code-blocks labeled by those arguments of f_{\cup} . Circuits defined by such functions constructed from cup-products of finitely many 1-cochains (three, in this case) lead to sparse, finite depth circuits [16, 55]. Moreover, such functions f_{\cup} naturally have the property that they vanish on 1-coboundaries: f_{\cup} vanishes if any of its three arguments is of the form $d^0(c)$ for $c \in C^0$, where d^0 is the coboundary map from C^0 to C^1 – equivalent to the matrix H_X^T . This condition is thus equivalent to f_{\cup} vanishing when any of its arguments corresponds to an X -type stabilizer (see Sec. 2.2) and is called *coboundary* invariance. The coboundary invariance property is essential to ensure that the circuit defined by f_{\cup} descends to a well-defined logical operation [55, 16] – intuitively, this is so that the action of f_{CCZ} on logical operators does not change upon adding stabilizers to the logical operators.

The formalism of [16] constructs cup-products on classical 2-term cochain complexes which satisfy certain sufficient conditions such that homological and balanced product complexes constructed from them (see supplementary material) are also equipped with an appropriate cup-product. This yields a trilinear function of the form in Eq. (20) on the product complexes associated with quantum CSS codes. Since tricycle codes are balanced products of classical Abelian group-algebra codes, these methods readily apply, which we review here. Note that for this to work, we require a mild technical condition that the check-weight of the classical codes is even (see [16] for details) – this is why we do not consider tricycle codes that are balanced products of classical group-algebra codes with weight 3 checks despite the lower resulting check weight.

To equip a two-term cochain complex with a cup-product, one must construct partitions of the 1-coboundaries known as *pre-orientations*. For a classical Abelian group-algebra code associated with the two-term cochain complex of Eq. (16) defined by an element $a \in \mathbb{F}_2[G]$, this amounts to choosing a partition of the group algebra element into smaller disjoint group-algebra elements

$$a = a_{in} + a_{out} + a_{free} \quad (21)$$

where $a_{in}, a_{out}, a_{free} \in \mathbb{F}_2[G]$. Different choices of partitions induce different cup-products on the classical code according to the rules in definition 5.2 of [16]. Given three such classical group algebra codes defined by elements $a, b, c \in \mathbb{F}_2[G]$, each with their respective in, out, and free partitions, the three-fold balanced product tricycle code can be equipped with a natural cup-product if the preorientations of the classical codes obey certain conditions. These conditions are listed in proposition 5.2 of [16] which we repeat here in a form that is adapted for group-algebra codes. Below, we will use $|a|$ to measure the weight of the group-algebra element a – i.e the number of group elements that appear in its expansion. We also write $a_1 \cap a_2$ for $a_1, a_2 \in \mathbb{F}_2[G]$ to denote the set of group elements that are common to both group-algebra elements. The conditions on the classical preorientation of the code defined by $a \in \mathbb{F}_2[G]$ are then (with the conditions on the b and c classical code preorientations defined identically):

$$|a_{in}| + |a_{out}| = 0 \bmod(2) \quad (22)$$

$$|a_{in} \cdot g \cap a_{free} \cdot h| = 0 \bmod(2) \quad \forall g, h \in G : g \neq h \quad (23)$$

$$|a_{out} \cdot g \cap a_{free} \cdot h| = 0 \bmod(2) \quad \forall g, h \in G : g \neq h \quad (24)$$

$$|a_{out} \cdot f \cap a_{free} \cdot g \cap a_{in} \cdot h| = 0 \bmod(2) \quad \forall f, g, h \in G : f \neq g \neq h, f \neq g \quad (25)$$

where the multiplication in the expressions above is in the group-algebra sense. For three classical group-algebra codes with preorientations that satisfy the above conditions, the balanced product yields a cup-product on the quantum code's cochain complex, and consequently produces a constant depth CCZ circuit of the form Eq. (20). We will not reproduce the details of how the quantum code's cup-product follows from the above pre-orientations, and refer the reader to [16] for details.

We call a preorientation *non-trivial* if either the ‘in’ or ‘out’ partitions are non-zero, since only these terms contribute to the cup-product – the ‘free’ partition has no effect besides excluding certain group elements from contributing. Our first technical result on cup-products for the cochain complexes of the $(w_X, w_Z) = (12, 8)$ check-weight tricycle codes we consider in this work is that any valid, non-trivial preorientation of the classical codes must have the ‘free’ partition equal to 0. This follows from the next theorem.

Theorem B.1. *A classical group-algebra code defined by a weight-4 group-algebra element $a \in \mathbb{F}_2[G]$ only has non-trivial preorientations satisfying the conditions in Eq. (22)-Eq. (25) if $a_{free} = 0$.*

Proof. Suppose $a_{free} \neq 0$ for the sake of contradiction. Since $|a| = 4$, Eq. (22) implies that the only non-trivial possibilities are $|a_{in}| = 0, 1, 2, 4$. If $|a_{in}| = 4$ then the statement follows trivially. If $|a_{in}| = 1$, Eq. (22) implies that $|a_{out}| = 1, |a_{free}| = 2$. In this case, let $a_{in} = x$ and $a_{free} = y + z$, where $x, y, z \in G$. By assumption of disjointness of the partitions, $x \neq y \neq z$. Equation Eq. (23) is now impossible to satisfy, as for any $g \in G$, $gx = hy$ for $h = gxy^{-1}$ and $gx = hz$ for $h = gxz^{-1}$. Thus, the RHS of Eq. (23) is always 1 if $a_{free} \neq 0$. Similar reasoning holds if $|a_{in}| = 2$. If $a_{in} = 0$, the same logic applies to a_{out} using Eq. (24) instead. \square

A consequence of this theorem is that for the tricycle codes considered in this paper, we may restrict our attention to preorientations of the classical codes with empty free partitions. The condition in Eq. (22) then implies that the only possibilities are $|a_{in}| = 1, |a_{out}| = 3$ (or vice-versa) and $|a_{in}| = |a_{out}| = 2$. Any such partition of a thus produces a valid non-trivial preorientation, as the remaining conditions Eq. (23)- Eq. (25) are trivially satisfied by empty ‘free’ partitions.

Next, we define the f_{CCZ} function for the quantum tricycle codes that arises from the cup product specified by a choice of preorientations on the constituent classical group-algebra codes. The structure of the cochain complex in Eq. (18) implies that we can partition the qubits of the code into three sectors of $|G|$ qubits each – see Appendix A. Within each sector, a qubit can be labelled by a group element. Given some order of the group elements, the notation g^i will thus be used to denote qubit g of the i -th sector ($i = I, II, III$). For the following, denote $\alpha_I \equiv a$, $\alpha_{II} \equiv b$, $\alpha_{III} \equiv c$ as the three group-algebra elements that specify the classical codes (this notation makes the expression below compact).

Proposition 2. Consider a tricycle code defined by group-algebra elements $\alpha_I, \alpha_{II}, \alpha_{III} \in \mathbb{F}_2[G]$ with respective ‘in’ and ‘out’ pre-orientations. The function f_{CCZ} specifying the transversal CCZ circuits in Sec. 2.2 is defined as

$$f_{CCZ}(p^i, q^j, r^k) = |p^{-1}\alpha_I^{in} \cap q^{-1}\alpha_J^{out}| \cdot |q^{-1}\alpha_J^{in} \cap r^{-1}\alpha_K^{out}| \cdot \delta_{i \neq j \neq k} \pmod{2} \quad (26)$$

where $i, j, k \in \{I, II, III\}$ label the sectors of the qubits p, q, r in the three code-blocks respectively, and $\delta_{i \neq j \neq k}$ indicates that $f_{CCZ} = 0$ if any two or more qubits from its arguments are in the same sector. If any partition in the above expression is empty, $f_{CCZ} = 0$ on these arguments.

Proof (informal). This definition follows from a straightforward but tedious computation of the cup-product on the balanced-product quantum code induced by the classical code cup-products. See section 5.3.2 of [16] for the case $i = I, j = II, k = III$. The other 5 possible orderings of i, j, k follow a similar computation, which can be combined into the compact expression in Eq. (26). \square

Note that the expression in Proposition 2 holds for any tricycle code, not just those constructed from weight-4 group-algebra elements. The $\delta_{i \neq j \neq k}$ structure is manifest in the illustrations of the circuits in Fig. 1, where no CCZ acts between qubits in the same sector across code-blocks. We can now elucidate how the ‘single-sector’ (SS) and ‘triple-sector’ (TS) circuits introduced in Sec. 2.2 emerge from the structure of f_{CCZ} . A single-sector circuit acting across sector I of block 1, sector II of block 2, and sector III as in Fig. 1 b) is constructed by choosing $\alpha_I^{in} = \alpha_I$ and $\alpha_{III}^{out} = \alpha_{III}$, with other partitions of α_I and α_{III} set to 0 and both partitions of α_{II} non-zero. This makes $f_{CCZ} = 0$ on any other combination of argument sectors. A triple-sector circuit instead has all ‘in’ and ‘out’ partitions of $\alpha_I, \alpha_{II}, \alpha_{III}$ non-zero. In a triple-sector circuit, gates involved between sectors $I - II - III$, $II - III - I$, and $III - I - II$ of the three blocks can be parallelized, while sectors $I - III - II$, $II - I - III$, and $III - II - I$ can be done in another set of parallelizable gates – these correspond to the orange and black gate layers in Fig. 1 c).

Using the expression in Eq. (26), we can analyze the depth of the resulting CCZ circuits.

Theorem B.2. All tricycle codes constructed from weight-4 group-algebra elements $\alpha_I, \alpha_{II}, \alpha_{III}$ have depth-18 code-space preserving CCZ circuits.

Proof. The depth 18 circuits are triple-sector circuits constructed by choosing any preorientations with $|\alpha_I^{in}| = 1$, $|\alpha_I^{out}| = 3$, $|\alpha_{II}^{in}| = 1$, $|\alpha_{II}^{out}| = 3$, $|\alpha_{III}^{in}| = 1$, $|\alpha_{III}^{out}| = 3$. Then, for fixed p^i , $|p^{-1}\alpha_I^{in} \cap q^{-1}\alpha_J^{out}| = 1$ for exactly 3 different q^j . For each such q^j , $|q^{-1}\alpha_J^{in} \cap r^{-1}\alpha_K^{out}| = 1$ in turn for exactly 3 different r^k . Thus, each distinct sector-triple i, j, k contributes 9 CCZ gates acting on each qubit in the sectors. Each sector of each code-block is involved in two such triples – for example, sector I of block 1 is involved in CCZ gates acting as $I - II - III$ and $I - III - II$ between code-blocks. Each such triple contributes 9 gates, leading to a total depth 18 circuit with the structure illustrated in Fig. 1 c). \square

Consequently, all tricycle codes in Table 1 have depth-18 CCZ circuits, constructed from any partition of the form described in the preceding proof. Using similar reasoning, one can show that larger circuit depths are possible. For example, a SS circuit with $|\alpha_I^{in}| = 4$, $|\alpha_{II}^{out}| = |\alpha_{II}^{in}| = 2$, $|\alpha_{III}^{out}| = 4$ with no further structure between the preorientations will generically lead to a depth $4 \times 2 \times 2 \times 4 = 64$ circuit. However, we are of course interested primarily in shorter depth CCZ circuits.

By imposing additional relations between the α group-algebra elements, this can be accomplished. We illustrate how this can be done to achieve a depth-4 SS circuit in the proof of the following theorem. Circuits with other attainable depths 8, 12, 16 for both SS and TS circuits are constructed using a very similar method.

Theorem B.3. *There exist tricycle codes constructed from weight-4 group algebra elements $\alpha_I, \alpha_{II}, \alpha_{III}$ which have depth-4 single-sector code-space preserving CCZ circuits.*

Proof. We derive conditions that $\alpha_I, \alpha_{II}, \alpha_{III}$ must satisfy to be compatible with such a circuit. We will consider preorientations with the single-sector circuit pattern $|\alpha_I^{in}| = 4$, $|\alpha_{II}^{out}| = |\alpha_{II}^{in}| = 2$, $|\alpha_{III}^{out}| = 4$ for the f_{CCZ} function in Eq. (26). Let us explicitly write out the group algebra elements as

$$\alpha_I^{in} = \alpha_I = a + b + c + d \quad (27)$$

$$\alpha_{II}^{out} = e + f \quad (28)$$

$$\alpha_{II}^{in} = g + h \quad (29)$$

$$\alpha_{III}^{out} = \alpha_{III} = i + j + k + l \quad (30)$$

for $a \dots l \in G$, and $a \neq b \neq c \neq d, e \neq f \neq g \neq h, i \neq j \neq k \neq l$. As discussed in the preceding paragraph, without any additional structure, these partitions would produce a depth 64 circuit. To be more explicit, this is because for every one of the 4 group elements in α_I^{in} and every one of the 2 group elements in α_{II}^{out} , the group structure implies that there are $p, q \in G$ that make the first intersection term in the expression for f_{CCZ} in Eq. (26) equal to 1. This gives a factor of 8 (p, q) pairs from the first term in the expression for f_{CCZ} , and the second term similarly gives a factor of 8 (q, r) pairs from considering the intersections of α_{III}^{out} and α_{II}^{in} . Therefore, to reduce the circuit depths, we must reduce the number of pairs p, q that make the first intersection term in Eq. (26) non-zero, and independently reduce the number of pairs q, r that do so for the second intersection term.

Consider imposing the following group relations between the components of α_I^{in} and α_{II}^{out} :

$$af = be \quad (31)$$

$$bf = ce \quad (32)$$

$$cf = de \quad (33)$$

Then, for any $p, q \in G$ such that $p^{-1}a = q^{-1}e$, the first equation implies that $p^{-1}b = q^{-1}f$ must also be true. Thus, the intersection is made even (i.e, 0 mod(2)) whenever a, e are involved in a non-trivial intersection of the first term in Eq. (26) by forcing b, f to simultaneously be involved in the intersection. This reduces the contribution from the first term in Eq. (26) towards the number of CCZ gates by 2. Thus, imposing only the very first relation results in a circuit of depth $6 \times 8 = 48$. Similarly imposing the second and third equations each reduce the first factor by 2 each by pairing group terms involved in non-trivial intersection. Thus, imposing all three relations in Eq. (31) leads to a circuit of depth $2 \times 8 = 32$. One may be tempted to further impose a fourth relation such as $df = ce$, but a quick calculation shows that satisfying all 4 equations is only possible if one of the

partitions is identically 0. Similarly, one can impose the following relations between α_{II}^{out} and α_{III}^{in} :

$$ih = gj \quad (34)$$

$$jh = gk \quad (35)$$

$$kh = gl \quad (36)$$

Each equation reduces the contribution from the second term in Eq. (26) from 8 by 2. Thus, imposing all 6 equations in Eq. (31) and Eq. (34) leads to a final circuit depth of $2 \times 2 = 4$. Finally, existence of tricycle codes with good parameters that are constructed from group-algebra elements satisfying these relations is demonstrated numerically, by sampling group algebra elements that constructively satisfy the above relations. See examples in Table 2.

□

The proof of Theorem B.3 demonstrates how we find tricycle codes with short-depth circuits. We frame the equations in Eq. (31) and Eq. (34) as linear systems over the integer powers of group-generators corresponding to each group element. Then, we row-reduce the system to determine which of the variables $a \cdots l$ are free. These free variables are then randomly sampled from a given group, determining the other involved group elements. We filter sampled codes by rate and distance, using the methods in Appendix D. Using a similar ‘pairing’ idea between group elements, one can similarly construct SS circuits and TS circuits of depth 8, 12, 16. For example, a SS circuit with depth 8, 12, or 16 can be constructed by enforcing a subset of the equations in Eq. (31) and Eq. (34). We do not present all the details here, but one enforces a desired number of pairwise relations between involved group elements as in Eq. (31) and Eq. (34) to reduce the contribution of terms in Eq. (26) appropriately. In the Table 5, we provide the partitions used to construct the codes in Table 2 that have CCZ circuits with depth shorter than 18.

$[[\mathbf{N}, \mathbf{K}, (\mathbf{D}_X, \mathbf{D}_Z)]]$	$(\mathbf{l}, \mathbf{m}, \mathbf{n})$	Depth	\mathbf{a}_{in}	\mathbf{a}_{out}	\mathbf{b}_{in}	\mathbf{b}_{out}	\mathbf{c}_{in}	\mathbf{c}_{out}
$[[135, 3, \leq 22, 8]]$	$(3, 3, 5)$	4	$1 + yz + y^2z^2 + z^3$	—	$1 + xz^3$	$z^3 + yz^4$	—	$xy + yz + yz^2 + x^2yz^3$
$[[405, 9, (\leq 27, 10)]]$	$(3, 5, 9)$	4	$1 + yz^2 + z^4 + z^8$	—	$y^4z + z^6$	$y^4 + y^4z^8$	—	$y^3 + yz + y^3z^2 + y^4z^5$
$[[135, 3, (\leq 27, 9)]]$	$(3, 3, 5)$	8	$1 + xz^3 + x^2z^4 + z^4$	—	$yz + y^2z^3$	$y + x^2yz^4$	—	$y + yz + y^2z^2 + z^4$
$[[405, 9, (\leq 29, 11)]]$	$(3, 5, 9)$	8	$1 + yz^7 + y^2z^3 + y^4z^6$	—	$yz^2 + z^7$	$xy^2z^8 + xy^4z^2$	—	$x + xyz^4 + xy^3z + xy^4z^5$

[[405, 9, ($\leq 37, 14$)]]	(3, 5, 9)	12	$1 + z + x^2y^2z^5 + x^2y^3z^6$	-	$xz^8 + xy^4z^2$	$x^2y^3z + x^2y^3z^2$	-	$z^5 + yz^2 + y^2z^8 + y^4z^8$
[[405, 9, ($\leq 27, 11$)]]	(3, 5, 9)	12	$1 + z3$	$x^2y^3z^3 + x^2y^4z^5$	$z^2 + y^3z^7 + y^4$	y^4z^8	$x^2y + x^2y^2z^2 + x^2y^3z^4$	x^2yz^4
[[375, 15, ($\leq 15, 10$)]]	(5, 5, 5)	16	$1 + y^2$	$x^3yz^4 + x^4y^4$	$x^2z^2 + x^3y^3z^3$	$x^3y^2z^2 + x^3y^4z^2$	$y^2z^3 + y^4z^3$	$xy + x^2y^4z$

Table 5: Polynomials of partitions used to construct codes in Table 2 (listed in the same order) with short-depth \overline{CCZ} circuit. Polynomials represent elements of the group algebra of $G = \mathbb{Z}_l \times \mathbb{Z}_m \times \mathbb{Z}_n$. A dash indicates that a partition is empty. Codes are constructed by imposing group element equations similar to Eq. (31) and Eq. (34) and randomly sets of sampling group algebra elements that satisfy these relations.

C Logical circuit optimization

In this section we discuss how the logical \overline{CCZ} circuits that produce the hypergraph magic states described in Sec. 2.2 can be optimized to maximize the yield of disjoint \overline{CCZ} magic-gates.

The logical connectivity is determined by the cohomology invariant f_{CCZ} function restricted to a basis of logical X -type operators for the three code-blocks. In cohomological terms, this is a basis for the first cohomology group $H^1(C)$ of the associated co-chain complex. Denote a choice of these bases as $\{[l_i^1]\}_{i=1\dots K}, \{[l_j^2]\}_{j=1\dots K}, \{[l_k^3]\}_{k=1\dots K}$ where the l_i are representative elements of $\ker(H_Z)$ and $[\cdot]$ denotes an equivalence class modulo elements of $\text{im}(H_Z^T)$. We then construct a $K \times K \times K$ binary 3-tensor corresponding to the restriction of f_{CCZ} to the logical operators:

$$T_{ijk}^{log} = f_{CCZ}(l_i^1, l_j^2, l_k^3) \in \mathbb{F}_2 \quad (37)$$

The tensor T^{log} encodes all the structure of the resulting logical circuit: $T_{ijk}^{log} = 1$ implies a \overline{CCZ} gate between the i -th logical qubit of the first code block, j -th logical qubit of the second block, and k -th logical qubit of the third block. Naturally, changing the logical basis of each block will change the connectivity of the resulting circuit and the associated hypergraph magic state, corresponding to a change of basis on each leg of the T^{log} tensor. We would like to be able to extract some number of disjoint \overline{CCZ} gates from the circuit defined by f_{CCZ} by choosing an appropriate basis of logical X operators for each code block. The maximum such number of disjoint \overline{CCZ} , K_{CCZ} , that are extractable from the circuit is equal to the *subrank* of T^{log} . Intuitively, the subrank of a binary tensor measures the size of the largest identity-like diagonal subtensor that can be embedded within the tensor [24, 48]. More formally, the subrank of the tensor T^{log} is the largest integer $r \geq 0$ such that there exist matrices $M^1, M^2, M^3 \in \mathbb{F}_2^{r \times K}$ that satisfy

$$(M^1 \otimes M^2 \otimes M^3) \cdot T^{log} = \mathbb{I}^{r \times r \times r} \bmod(2) \quad (38)$$

where $\mathbb{I}^{r \times r \times r}$ is the $r \times r \times r$ tensor with 1s on the diagonal and 0 everywhere else. Equivalently, we can express this in components as

$$\sum_{i,j,k} T_{ijk}^{\log} M_{a,i}^1 M_{b,j}^2 M_{c,k}^3 = \mathbb{1}_{a=b=c \bmod(2)} \quad a, b, c \in [1 \cdots r] \quad (39)$$

The M matrices can be viewed as change of basis matrices such that rows of M define logical new logical operators in a different basis that produces r disjoint \overline{CCZ} gates. In particular, the optimal choice of r logical operators for the I -th code block is given by $\{\sum_j M_{a,j}^I (l_a^I)_j\}_{a=1 \dots r}$. The remaining $K - r$ logicals are found by choosing any set of logical operators that are linearly independent from the first r . These $K - r$ logicals are treated as gauge logical qubits, to be initialized in the $|\bar{0}\rangle$ state – see the discussion at the end of Sec. 2.2.

Unfortunately, finding the subrank r and the associated bases M^1, M^2, M^3 is a problem that is widely believed to be NP-Hard, even over the real numbers [48]. In this work, we find sub-optimal solutions using a Mixed-Integer-Programming (MIP) method – we use the Gurobi Python package for this task [38]. We first find a set of initial logical operators numerically using row-reduction over \mathbb{F}_2 . For fixed r we then treat the $3rK$ entries of M^1, M^2, M^3 as binary variables for the integer program, and enforce the condition in Eq. (39) as a set of integer constraints which involve another $2r^3$ many slack variables. The complexity of the integer program therefore grows dramatically with r . We iterate from $r = 0$ to increasing values of r until the MIP solver converges or is unable to find a feasible solution within time constraints. This leads to the reported values of K_{CCZ} in Sec. 2.2. An important direction for future work is to find tailored optimization heuristics for the binary tensor subrank problem to extract larger values of K_{CCZ} , significantly improving the throughput of \overline{CCZ} type magic states from the hypergraph magic states produced by our circuits.

D Determining code distances

We use three distinct methods to either find the exact distances or determine high statistical confidence estimates of the distances of tricycle codes.

The first method is a Mixed-Integer-Program (MIP). This involves first using Gaussian row-reduction over \mathbb{F}_2 to find a basis of logical X and Z operators L_X and L_Z independently for a given code. One then formulates the low-weight logical operator search as a mixed-integer-program by iterating over the basis of logical operators. For example, to find d_X , for the i^{th} logical operator $l_i \in L_Z$, we minimize the hamming weight of candidate bitstring solutions b under the constraints $H_Z b = 0 \bmod(2)$ and $b^T l_i = 1 \bmod(2)$ where the latter constraint enforces that b corresponds to an X -type logical operator that anticommutes with the i^{th} logical Z operator. The minimum weight logical operator is then found after iterating over all l_i if the solver converges within time constraints. We used the Gurobi [38] package in Python for this task.

We also sometimes use the shortest-error search method provided in the STIM package [32] combined with the PySat package [46] to directly formulate the problem of finding code distances as a Boolean constraint satisfaction (SAT) problem. For certain codes, we found that this method converged while the previous MIP method times out within time constraints, or vice-versa.

The MIP and SAT methods are not readily useful for the larger codes we consider in this work, and sometimes do not converge in one basis even for smaller codes, as in general, finding the exact

distance of a linear code is known to be *NP*-Hard. In these cases, we estimate the minimum distance of a CSS quantum code using a Monte Carlo algorithm that performs structured sampling over the space of low-weight logical operators. The algorithm is based on the information-set algorithm of [52] for classical linear codes, with the additional step that one has to remove low-weight codewords belonging to the row-space of the opposite parity check matrix. We note that the algorithm we use is essentially identical to that of the QDistRnd package [68] that is provided in the GAP computational algebra programming language. We developed an independent implementation in the python programming language. We briefly summarize the algorithm as well as the empirical probability of success estimates derived for the QDistRnd algorithm.

We discuss how to estimate d_Z , with the analysis for d_X being identical with the parity check matrices swapped. The objective is to find a nonzero vector $c \in \ker(H_X)$ such that $c \notin \text{rowspace}(H_Z)$, with minimal Hamming weight. The algorithm proceeds by first computing a basis G for the nullspace $\ker(H_X)$ using row-reduction over \mathbb{F}_2 . In each Monte Carlo trial, a random column permutation π is applied to the columns of G , followed by row reduction (forward elimination) to produce a low-weight generating set for $\ker(H_X)$. The inverse permutation π^{-1} is then applied to return to the original coordinate system. Rows of the resulting matrix that are linearly independent of the rows of H_Z are retained as candidate logical operators – this is once again determined using efficient row-reduction over \mathbb{F}_2 . The smallest observed weight among all valid logical operators encountered over many trials is reported as the estimated distance.

To assess the reliability of the distance estimate, we track the number of rediscoveries of each distinct minimum-weight logical operator over N trials. Let m denote the number of distinct minimum-weight vectors found, and let n_i be the number of times the i -th one is observed. We define the average rediscovery count as

$$\langle n \rangle = \frac{1}{m} \sum_{i=1}^m n_i.$$

Assuming that each trial samples a minimum-weight codeword independently and with equal probability $\lambda > 0$, the number of times each such codeword is found follows a Poisson distribution with mean $N\lambda$. Under this model, the probability that *no* minimum-weight codeword is discovered in N trials is at most

$$P_{\text{fail}} \leq \exp(-\langle n \rangle),$$

where $\langle n \rangle \approx N\lambda$. This gives a conservative upper bound on the probability of missing the true minimum distance. In particular, when $\langle n \rangle \gg 1$, the failure probability becomes exponentially small.

To further evaluate sampling quality, we test whether the distribution of rediscovery counts $\{n_i\}$ is consistent with a uniform multinomial distribution. If each minimum-weight codeword is equally likely to be sampled, the frequencies $\{n_i\}$ should follow a multinomial distribution with equal probabilities. Deviations from this uniformity are detected using a Pearson chi-squared test. A small associated p-value indicates uneven sampling, suggesting either bias in the heuristic or incomplete exploration of the codeword space. In the main text, we only report the distance found from this method as exact if the returned confidence $1 - P_{\text{fail}} > 0.99$ and if the p-value associated with the chi-squared test is > 0.1 . To ensure reliability of the hypothesis test, we also only infer a p-value from the chi-squared test if at least 2 distinct minimum weight code-words are found, and if at least 5 occurrences of each codeword are found. In all other cases, we report the estimated

distances as an upper bound, although the noise simulations in Sec. 2.4 show that noise suppression is compatible with code distances that are equal or near these estimates.

E Numerical details of noise simulations

We provide further details on the implementation of our circuit-level noise simulations.

We simulate syndrome extraction circuits for both X and Z checks of the tricycle codes. Each simulation begins by initializing the data qubits in the appropriate basis, followed by multiple cycles of syndrome extraction. At each cycle, fresh ancilla qubits are initialized, entangled with the data via two-qubit gates, and subsequently measured to extract the stabilizer values.

We consider two types of simulations: (1) single-shot simulations in the Z basis, and (2) fault-tolerant d -round simulations in the X basis, where the syndrome extraction circuit is repeated for d cycles prior to decoding, with d taken as the upper bound on the code distance.

For both single-shot Z -basis and d -round X -basis simulations, we employ a coloration circuit for syndrome extraction. While we explored various permutations of the entangling gate order within the circuit, only negligible improvements in performance were found. Thus, a random coloration circuit is used in our results. We note that more exhaustive searches over gate orderings could further improve performance, for example by suppressing hook errors.

Decoding is performed using a belief-propagation with ordered statistics decoding (BP+OSD) scheme as presented in Ref. [65]. To enable circuit-level decoding, we map each syndrome extraction circuit to a spacetime code: checks of the spacetime code correspond to parities of stabilizer measurements across consecutive rounds, and the code qubits represent distinct fault locations (e.g., a two-qubit gate error at a specific location in space and time). Formally, for each round, the value of a stabilizer at time t is $m_t \in \{0, 1\}$; the detector value is defined as $d_t := m_t + m_{t-1} \pmod{2}$. Detectors are associated with the checks of the spacetime code, and the code qubits are assigned to circuit fault locations. A qubit is included in the support of a check if a fault at that location alone would flip the outcome of the associated detector.

All circuits were constructed using Stim [32], and BP+OSD decoding was implemented using the tools from Ref. [72, 71]. For the X -basis d -rounds simulations, we apply a BP+OSD decoder to the full spacetime code with 10000 maximum iterations of min-sum BP and min-sum scaling factor of 0. We used OSD-CS of order 10. For the Z -basis single-shot simulations, we decode each window of three cycles using a BP decoder with maximum iterations set to $\# \text{ qubits} / 5$ and min-sum scaling factor of 0.9. To decode the final transversal measurement we use BP+OSD with maximum iterations set to $\# \text{ qubits} / 5$, min-sum scaling factor of 0.9 and OSD-E of order 10. Although we did not attempt extensive hyperparameter optimization, preliminary trials suggest that targeted tuning of BP+OSD parameters could produce significant gains in logical error rate.

F Optimal-depth syndrome extraction circuits

We provide a constructive proof of the following theorem.

Theorem F.1. *For tricycle codes defined by $\mathbf{A} = \sum_{i=1}^{w_a} \mathbf{A}_i$, $\mathbf{B} = \sum_{i=1}^{w_b} \mathbf{B}_i$, and $\mathbf{C} = \sum_{i=1}^{w_c} \mathbf{C}_i$ where w_a , w_b , and w_c are even, there exists syndrome extraction circuits with CNOT depth $w_a + w_b + w_c$.*

Proof. Let $X \rightarrow \mathbf{A}_i^T(D_1)$ denote CNOTs from check sector X to data sector D_1 according to permutation \mathbf{A}_i^T . The arrow indicates the CNOT direction: from each qubit j in X to qubit k in D_1 whenever the (j, k) entry of \mathbf{A}_i^T is 1. Since \mathbf{A}_i^T are permutation matrices, the CNOTs are disjoint and can be executed in parallel.

We schedule all CNOTs in five stages, with $w_a + w_b + w_c$ layers in total (square brackets indicate groups of CNOTs in the same layer):

- (1) for $1 \leq i \leq w_c/2$, apply $[\mathbf{C}_{i+w_c/2}(D_1) \rightarrow Z_1, \mathbf{C}_{i+w_c/2}(D_2) \rightarrow Z_2, X \rightarrow \mathbf{C}_i^T(D_3)]$;
- (2) for $1 \leq i \leq w_b/2$, apply $[\mathbf{B}_{i+w_b/2}(D_1) \rightarrow Z_3, X \rightarrow \mathbf{B}_i^T(D_2), \mathbf{B}_{i+w_b/2}(D_3) \rightarrow Z_2]$;
- (3) for $1 \leq i \leq w_a$, apply $[X \rightarrow \mathbf{A}_i^T(D_1), \mathbf{A}_i(D_2) \rightarrow Z_3, \mathbf{A}_i(D_3) \rightarrow Z_1]$;
- (4) for $1 \leq i \leq w_b/2$, apply $[\mathbf{B}_i(D_1) \rightarrow Z_3, X \rightarrow \mathbf{B}_{i+w_b/2}^T(D_2), \mathbf{B}_i(D_3) \rightarrow Z_2]$;
- (5) for $1 \leq i \leq w_c/2$, apply $[\mathbf{C}_i(D_1) \rightarrow Z_1, \mathbf{C}_i(D_2) \rightarrow Z_2, X \rightarrow \mathbf{C}_{i+w_c/2}^T(D_3)]$.

It remains to verify that this schedule measures the stabilizers while preserving logical operators. The CNOTs' effects can be tracked using a stabilizer table; since CNOTs do not mix X and Z parts, the action on each part can be analyzed separately. We focus on the X-part; the Z-part is similar.

Consider the stabilizer table extended with an arbitrary logical Pauli X, supported on 1-entries of row vectors u , v , and w . The circuit is correct if the CNOTs yield the expected outcome:

$$\left[\begin{array}{c|ccccccc} X & D_1 & D_2 & D_3 & Z_1 & Z_2 & Z_3 \\ \hline \mathbf{I} & 0 & 0 & 0 & 0 & 0 & 0 \\ 0 & \mathbf{A}^T & \mathbf{B}^T & \mathbf{C}^T & 0 & 0 & 0 \\ 0 & u & v & w & 0 & 0 & 0 \end{array} \right] \rightarrow \left[\begin{array}{c|ccccccc} X & D_1 & D_2 & D_3 & Z_1 & Z_2 & Z_3 \\ \hline \mathbf{I} & \mathbf{A}^T & \mathbf{B}^T & \mathbf{C}^T & 0 & 0 & 0 \\ \mathbf{I} & \mathbf{A}^T & \mathbf{B}^T & \mathbf{C}^T & 0 & 0 & 0 \\ 0 & u & v & w & 0 & 0 & 0 \end{array} \right] \quad (41)$$

At stage 1, the CNOTs from X to D_3 add rows from column X to those in column D_3 , permuted by each \mathbf{C}_i^T . Let $\mathbf{C}_{<}^T := \sum_{i=1}^{w_c/2} \mathbf{C}_i^T$ and $\mathbf{C}_{>}^T := \sum_{i=1+w_c/2}^{w_c} \mathbf{C}_i^T$; these CNOTs correspond to right-multiplying column X by $\mathbf{C}_{<}^T$ and accumulating into D_3 . The other two CNOT groups propagate from data sectors to Z-checks. As each \mathbf{C}_i is a permutation matrix, $\mathbf{C}_i(D_1) \rightarrow Z_1$ is equivalent to $D_1 \rightarrow \mathbf{C}_i^T(Z_1)$; we use this equivalence below. Thus, the CNOT action right-multiplies D_1 and D_2 by $\mathbf{C}_{>}^T$ and accumulates the results to Z_1 and Z_2 , respectively. After stage 1, the table becomes

$$\left[\begin{array}{c|ccc|ccc} \mathbf{I} & 0 & 0 & \mathbf{C}_{<}^T & 0 & 0 & 0 \\ 0 & \mathbf{A}^T & \mathbf{B}^T & \mathbf{C}^T & \mathbf{A}^T \mathbf{C}_{>}^T & \mathbf{B}^T \mathbf{C}_{>}^T & 0 \\ 0 & u & v & w & u \mathbf{C}_{>}^T & v \mathbf{C}_{>}^T & 0 \end{array} \right].$$

After stage 2, the table becomes

$$\left[\begin{array}{c|ccc|ccc} \mathbf{I} & 0 & \mathbf{B}_{<}^T & \mathbf{C}_{<}^T & 0 & \mathbf{C}_{<}^T \mathbf{B}_{>}^T = \mathbf{B}_{>}^T \mathbf{C}_{<}^T & 0 \\ 0 & \mathbf{A}^T & \mathbf{B}^T & \mathbf{C}^T & \mathbf{A}^T \mathbf{C}_{>}^T & \mathbf{B}^T \mathbf{C}_{>}^T + \mathbf{C}_{>}^T \mathbf{B}_{>}^T & \mathbf{B}_{>}^T \mathbf{C}^T & \mathbf{A}^T \mathbf{B}_{>}^T \\ 0 & u & v & w & u \mathbf{C}_{>}^T & v \mathbf{C}_{>}^T + w \mathbf{B}_{>}^T & u \mathbf{B}_{>}^T & \end{array} \right],$$

where the equalities hold since all polynomial terms in \mathbf{A} , \mathbf{B} , and \mathbf{C} commute. We will use this property throughout and consistently write products of terms in dictionary order.

After stage 3, the table becomes

$$\left[\begin{array}{c|ccc|ccc} \mathbf{I} & \mathbf{A}^T & \mathbf{B}_{<}^T & \mathbf{C}_{<}^T & \mathbf{A}^T \mathbf{C}_{<}^T & \mathbf{B}_{>}^T \mathbf{C}_{<}^T & \mathbf{A}^T \mathbf{B}_{<}^T \\ 0 & \mathbf{A}^T & \mathbf{B}^T & \mathbf{C}^T & \mathbf{A}^T \mathbf{C}_{>}^T + \mathbf{A}^T \mathbf{C}^T & \mathbf{B}^T \mathbf{C}_{>}^T + \mathbf{B}_{>}^T \mathbf{C}^T & \mathbf{A}^T \mathbf{B}_{>}^T + \mathbf{A}^T \mathbf{B}^T \\ 0 & u & v & w & u \mathbf{C}_{>}^T + w \mathbf{A}^T & v \mathbf{C}_{>}^T + w \mathbf{B}^T & u \mathbf{B}_{>}^T + v \mathbf{A}^T \end{array} \right].$$

After stage 4, the table becomes

$$\left[\begin{array}{c|ccc|ccc} \mathbf{I} & \mathbf{A}^T & \mathbf{B}^T & \mathbf{C}_{<}^T & \mathbf{A}^T \mathbf{C}_{<}^T & \mathbf{B}_{>}^T \mathbf{C}_{<}^T & \mathbf{A}^T \mathbf{B}_{<}^T + \mathbf{A}^T \mathbf{B}_{<}^T = 0 \\ 0 & \mathbf{A}^T & \mathbf{B}^T & \mathbf{C}^T & \mathbf{A}^T \mathbf{C}_{>}^T + \mathbf{A}^T \mathbf{C}^T & \mathbf{B}^T \mathbf{C}_{>}^T + \mathbf{B}_{>}^T \mathbf{C}^T & \mathbf{A}^T \mathbf{B}_{>}^T + \mathbf{A}^T \mathbf{B}_{>}^T = 0 \\ 0 & u & v & w & u \mathbf{C}_{>}^T + w \mathbf{A}^T & v \mathbf{C}_{>}^T + w \mathbf{B}^T & u \mathbf{B}_{>}^T + v \mathbf{A}^T \end{array} \right],$$

where the equalities hold since the addition is modulo 2.

Finally, after stage 5, the table becomes

$$\left[\begin{array}{c|ccc|ccc} \mathbf{I} & \mathbf{A}^T & \mathbf{B}^T & \mathbf{C}^T & 0 & 0 & 0 \\ 0 & \mathbf{A}^T & \mathbf{B}^T & \mathbf{C}^T & 0 & 0 & 0 \\ 0 & u & v & w & u \mathbf{C}^T + w \mathbf{A}^T = 0 & v \mathbf{C}^T + w \mathbf{B}^T = 0 & u \mathbf{B}^T + v \mathbf{A}^T = 0 \end{array} \right],$$

where the equalities hold since any logical Pauli X commutes with Z-checks, i.e., $[u \ v \ w] H_z^T = 0$. \square

The above theorem applies to all codes presented in the main text. For other cases, let $W = w_a + w_b + w_c$ and $V = |\{w \in \{w_a, w_b, w_c\} \mid w \text{ is even}\}|$. Our scheduling method produces the following result, which is at most two CNOT layers from optimal.

Corollary F.1.1. *For tricycle codes with $V = 0, 1, 2$, and 3, there exists syndrome extraction circuits with CNOT depth W , W , $W + 1$, and $W + 2$, respectively.*

Proof. Theorem F.1 covers $V = 0$. For $V = 1$, assign the odd-weight polynomial as \mathbf{A} , and the previous proof still applies. For $V = 2$, assign the odd-weight polynomials as \mathbf{A} and \mathbf{C} . Modifying stages 1 and 5 of in Eq. (40) as follows suffices:

- (1) apply $X \rightarrow \mathbf{C}_1^T(D_3)$;
- for $1 \leq i \leq \lfloor w_c/2 \rfloor$, apply $[\mathbf{C}_{i+\lfloor w_c/2 \rfloor}(D_1) \rightarrow Z_1, \mathbf{C}_{i+\lfloor w_c/2 \rfloor}(D_2) \rightarrow Z_2, X \rightarrow \mathbf{C}_{1+i}^T(D_3)]$;
- (5) for $1 \leq i \leq \lfloor w_c/2 \rfloor$, apply $[\mathbf{C}_i(D_1) \rightarrow Z_1, \mathbf{C}_i(D_2) \rightarrow Z_2, X \rightarrow \mathbf{C}_{1+i+\lfloor w_c/2 \rfloor}^T(D_3)]$;
- apply $[\mathbf{C}_{w_c}(D_1) \rightarrow Z_1, \mathbf{C}_{w_c}(D_2) \rightarrow Z_2]$.

Thus, stages 1 and 5 now take $w_c + 1$ layers. For $V = 3$, modify stages 2 and 4 in a similar way. \square

Following Ref. [13], counting both initialization and measurement of check qubits as unit depth, our construction gives the following results.

Corollary F.1.2. *For tricycle codes with $V = 0, 1, 2$, and 3, there exists M -cycle syndrome extraction circuits with depth $(W+2)M$, $(W+2)M$, $(W+2)M+1$, and $(W+3)M+1$, respectively.*

Proof. For $V = 0$ and $V = 1$, initialization precedes and measurement follows the CNOT layers each cycle, adding two units per cycle. For $V = 2$ and $V = 3$, as illustrated in Fig. 6a, X-check measurement can be parallelized with the final CNOT layer, and Z-check initialization with the first layer in Eq. (42), resulting in the stated depths. \square

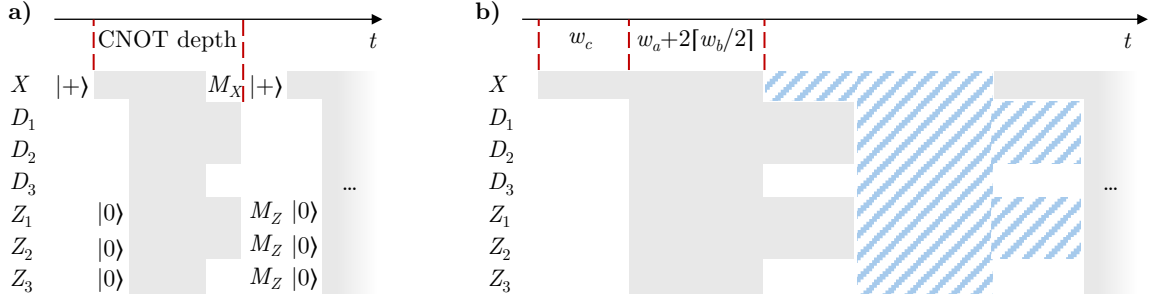


Figure 6: **Syndrome extraction circuit for multiple cycles:** (a) When w_c is odd, X-check measurements can overlap with the last CNOT layer, and Z-check initialization can overlap with the first CNOT layer. (b) Staggered scheduling with separate check qubits for even and odd cycles. Solid and hatched patterns indicate CNOTs for even and odd cycles, respectively. Measurement and initialization for one cycle can overlap with the CNOTs of the other cycle.

With two sets of check qubits, we use one set for odd cycles and the other set for even cycles.

Theorem F.2. *Given two sets of check qubits, for tricycle codes with $V = 0, 1, 2$, and 3 , there exists M -cycle syndrome extraction circuits with CNOT depth $WM + w_c$, $WM + w_c$, $WM + w_c$, and $(W + 1)M + w_c$, respectively.*

Proof. Adapt stages 1 and 5 in Eq. (40) as follows:

- (1) for $1 \leq i \leq w_c$, apply $[\mathbf{C}_i(D_1) \rightarrow Z'_1, \mathbf{C}_i(D_2) \rightarrow Z'_2, X \rightarrow \mathbf{C}_i^T(D_3)]$;
- (5) for $1 \leq i \leq w_c$, apply $[\mathbf{C}_i(D_1) \rightarrow Z_1, \mathbf{C}_i(D_2) \rightarrow Z_2, X' \rightarrow \mathbf{C}_i^T(D_3)]$;

(43)

where the prime indicates check qubits for the other cycle. This yields a staggered circuit (Fig. 6b) similar to the construction for hypergraph product codes in Ref. [95]. If at least one polynomial has even weight, assign it as \mathbf{B} ; if $V = 3$, revise stages 2 and 4 similarly to Eq. (42). \square

The above results naturally adapt to bicycle codes. For example, when $w_a = w_b = 3$, the circuits for bivariate bicycle codes in Ref. [13] are reproduced.

G Neutral atom array architecture and rearrangement procedure

To concretely specify the atom rearrangement procedure, we consider the reference architecture shown in Fig. 7, primarily based on settings from recent experiments [4, 5, 23]. The neutral atom array features multiple zones for different functions: an entangling zone for CNOT operations, a storage zone for densely packed atoms, a measurement zone for imaging, and a reservoir for fresh atoms. For our purposes, we focus on the entangling and storage zones.

SLM traps are present throughout these zones, and atoms can be rearranged by AOD between SLM grids, subject to AOD order constraints. Parts of the storage zone adjacent to the entangling zone serve as workspaces, where sector permutations occur before each CNOT layer. We further divide the workspace into regions S_i , each supporting permutation of a sector, and each containing

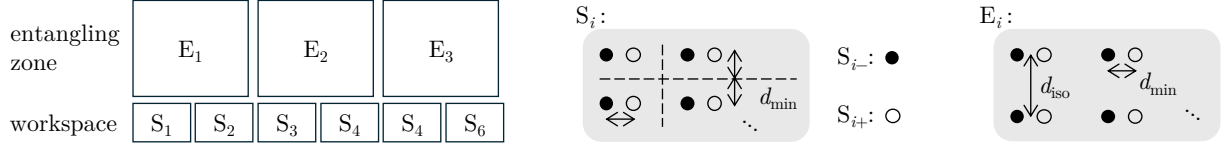


Figure 7: **Reference neutral atom array architecture.** Rydberg interactions are enabled only within the entangling zone. We slice the zones to regions E_i and S_i , each one can store a sector. Each region contains two trap arrays (dots/- and circles/+) to facilitate sector permutation or parallel CNOTs. In the workspace, traps are spaced by twice the minimal distance permitted by optical resolution, d_{\min} , allowing qubits to move between traps along dashed paths. In the entangling zone, traps are spaced so that qubit pairs involved in parallel CNOTs are separated by a distance to sufficiently isolate the Rydberg interaction, d_{iso} .

two SLM trap arrays: S_{i-} (dots) and S_{i+} (circles), each shaped like a sector (e.g., n_y rows by $n_x n_z$ columns as in Fig. 5b). These arrays are just labels; physically, all SLM traps are generated together.

For example, a y -cycling permutation of $1 \leq m < n_y$ units for a sector in S_{i-} requires two AOD movements: shifting rows $1, \dots, n_y - m$ in S_{i-} down to rows $m + 1, \dots, n_y$ in S_{i+} ; and the wrap-around, shifting rows $n_y - m + 1, \dots, n_y$ up to rows $1, \dots, m$ in S_{i+} . After cycling, the sector is entirely in S_{i+} . Minimizing the SLM trap spacing in S_i enables faster permutation, which is limited by the optical resolving distance, d_{\min} . The vertical spacing of S_{i+} is set to $2d_{\min}$, allowing qubits to traverse the region along the dashes; and the horizontal spacing is $3d_{\min}$ to additionally ensure sufficient separation between S_{i-} and S_{i+} .

Each entangling region E_i contains two arrays, E_{i-} and E_{i+} . To perform parallel CNOTs, one sector is positioned in E_{i-} , the other in E_{i+} , and a global Rydberg laser pulse is applied. We refer to the AOD movement from workspace to the entangling zone as fetching, and the movement back as put-back. To ensure that only intended pairs interact, the trap spacing in E_i is set to at least d_{iso} , a distance to sufficiently isolate Rydberg interactions. For example, with $d_{\min} = 2 \mu\text{m}$ and $d_{\text{iso}} = 10 \mu\text{m}$ [4], each E_i is about twice as wide as each S_j .

We now explicitly describe the atom rearrangement procedure outlined in Sec. 2.5, based on the reference architecture. For initialization, place D_1 in E_1 , D_2 in E_2 , D_3 in E_3 , Z_3 in S_2 , Z_1 in S_3 , Z_2 in S_4 , and X in S_5 . To implement the first layer, perform:

- Permute X (relabeling): $\mathbf{C}_1 \mathbf{1}(S_5)$;
- Permute Z (relabeling): $\mathbf{C}_3^T \mathbf{1}[S_2, S_3, S_4]$;
- Fetch X , Z_1 and Z_2 : $[S_5 \rightarrow E_3, S_3 \rightarrow E_1, S_4 \rightarrow E_2]$;
- CNOTs: $[\mathbf{C}_3(D_1) \rightarrow Z_1, \mathbf{C}_3(D_2) \rightarrow Z_2, X \rightarrow \mathbf{C}_1^T(D_3)]$;
- Put back X , Z_1 and Z_2 : $[E_3 \rightarrow S_5, E_1 \rightarrow S_3, E_2 \rightarrow S_4]$.

Here, ‘permute Z ’ refers to simultaneous permutation of all three Z sectors. Permutations are denoted as $\sigma' \sigma^T(S_i)$, where σ is the current permutation and σ' the target, within region S_i .

Specifically for this first layer, since the X and Z sectors are still fresh, we can relabel their qubits instead of performing physical permutations. Fetching and put-back notation indicate initial and final regions for AOD movements, potentially involving sequential moves and grid changes. We do not specify which array within a region is used, as either suffices. CNOT notation follows previous sections, and parallelized movements are listed in square brackets. Notably, fetching and put-back for X and Z sectors can be combined for this layer.

The full implementation of the syndrome extraction circuit in Eq. (40) proceeds similarly. For convenience, the permutation notation is slightly abused: when $i = 1$, in expressions like $\mathbf{C}_{i+w_c/2}^T \mathbf{C}_{i-1+w_c/2} [S_2, S_3, S_4]$, the second matrix refers to the prior permutation on those sectors (e.g., identity for stage (1)), not literally $\mathbf{C}_{w_c/2}$. The accompanying video demonstrates an instance with $n_x = n_y = n_z = 3$ and $\mathbf{A} = yz^2 + x^2z + x^2y + x^2y^2z$, $\mathbf{B} = yz^2 + xy + x^2y + x^2y^2z$, and $\mathbf{C} = 1 + xz^2 + x^2y^2 + x^2y^2z$.

- (1) For $1 \leq i \leq w_c/2$, permute X : $\mathbf{C}_i \mathbf{C}_{i-1}^T [S_5]$; permute Z : $\mathbf{C}_{i+w_c/2}^T \mathbf{C}_{i-1+w_c/2} [S_2, S_3, S_4]$; fetch Z_1, Z_2 , and X : $[S_3 \rightarrow E_1, S_4 \rightarrow E_2, S_5 \rightarrow E_3]$; CNOTs: $[\mathbf{C}_{i+w_c/2}(D_1) \rightarrow Z_1, \mathbf{C}_{i+w_c/2}(D_2) \rightarrow Z_2, X \rightarrow \mathbf{C}_i^T(D_3)]$; put back Z_1, Z_2 , and X : $[E_1 \rightarrow S_3, E_2 \rightarrow S_4, E_3 \rightarrow S_5]$.
- (2) For $1 \leq i \leq w_b/2$, permute X : $\mathbf{B}_i \mathbf{B}_{i-1}^T [S_5]$; permute Z : $\mathbf{B}_{i+w_c/2}^T \mathbf{B}_{i-1+w_c/2} [S_2, S_3, S_4]$; fetch X : $S_5 \rightarrow E_2$; fetch Z_3 and Z_2 : $[S_2 \rightarrow E_1, S_4 \rightarrow E_2]$; CNOTs: $[\mathbf{B}_{i+w_b/2}(D_1) \rightarrow Z_3, X \rightarrow \mathbf{B}_i^T(D_2), \mathbf{B}_{i+w_b/2}(D_3) \rightarrow Z_2]$; put back X : $E_2 \rightarrow S_5$; put back Z_1 and Z_2 : $[E_1 \rightarrow S_2, E_2 \rightarrow S_4]$.
- (3) For $1 \leq i \leq w_a$, permute X : $\mathbf{A}_i \mathbf{A}_{i-1}^T [S_5]$; permute Z : $\mathbf{A}_i^T \mathbf{A}_{i-1} [S_2, S_3, S_4]$; fetch X : $S_5 \rightarrow E_1$; fetch Z_3 and Z_1 : $[S_2 \rightarrow E_2, S_3 \rightarrow E_3]$; CNOTs: $[X \rightarrow \mathbf{A}_i^T(D_1), \mathbf{A}_i(D_2) \rightarrow Z_3, \mathbf{A}_i(D_3) \rightarrow Z_1]$; put back X : $E_1 \rightarrow S_5$; put back Z_3 and Z_1 : $[E_2 \rightarrow S_2, E_3 \rightarrow S_3]$.
- (4) For $1 \leq i \leq w_b/2$, permute X : $\mathbf{B}_{i+w_b/2} \mathbf{B}_{i-1+w_b/2}^T [S_5]$; permute Z : $\mathbf{B}_i^T \mathbf{B}_{i-1} [S_2, S_3, S_4]$; fetching and put-back are the same as (2).
- (5) For $1 \leq i \leq w_c/2$, permute X : $\mathbf{C}_{i+w_c/2} \mathbf{C}_{i-1+w_c/2}^T [S_5]$; permute Z : $\mathbf{C}_i^T \mathbf{C}_{i-1} [S_2, S_3, S_4]$; fetching and put-back are the same as (1).

For $w_a = w_b = w_c = 4$, the above procedure results in 22 sector permutations (with relabeling used in the first layer) and 40 fetch/put-back operations. While the scheme is general and structured, inefficiencies may arise from always restoring sectors to their original locations and exclusively permuting check sectors instead of data sectors. For example, in (3), since $\mathbf{A}_i(X) \rightarrow D_1$ is equivalent to $X \rightarrow \mathbf{A}_i^T(D_1)$, permuting D_1 instead of X may allow both Z sectors and D_1 to be permuted in parallel by $\mathbf{A}_i^T \mathbf{A}_{i-1}$. However, it is the change in permutation, $\sigma' \sigma^T$, and not the polynomial term σ itself, that enables such parallelization. If two sectors share σ' but have different σ , their permutations still cannot be merged, so a more careful analysis is needed to assess the potential benefits.

There is also flexibility to reorder CNOT layers or combine different CNOT groups into parallel layers, which changes $\sigma' \sigma^T$ between layers. This sometimes results in cancellations, reducing the need for certain x -, y -, or z -cycling steps, and can be formulated as a variant of the traveling salesman problem and be solved optimally for small instances.

It is also valuable to investigate ‘torus-like layout’ strategies, where sectors are interspersed not only during entangling gates but also during permutations, provided that there are polynomial terms

corresponding to nearest-neighbor interactions [13, 91]. Further optimization of sector layout and movement may be possible by mapping the problem to mathematical programming [87, 86, 89, 82] or graph theory formulations [88, 56, 81].

References

- [1] P. Aliferis, F. Brito, D. P. DiVincenzo, J. Preskill, M. Steffen, and B. M. Terhal. Fault-tolerant computing with biased-noise superconducting qubits: a case study. *New Journal of Physics*, 11(1):013061, 2009.
- [2] G. Baranes, M. Cain, J. P. Bonilla Ataides, D. Bluvstein, J. Sinclair, V. Vuletic, H. Zhou, and M. D. Lukin. Leveraging atom loss errors in fault tolerant quantum algorithms. *arXiv preprint arXiv:2502.20558*, 2025.
- [3] M. J. Bedalov, M. Blakely, P. D. Buttler, C. Carnahan, F. T. Chong, W. C. Chung, D. C. Cole, P. Goiporia, P. Gokhale, B. Heim, G. T. Hickman, E. B. Jones, R. A. Jones, P. Khalate, J.-S. Kim, K. W. Kuper, M. T. Lichtman, S. Lee, D. Mason, N. A. Neff-Mallon, T. W. Noel, V. Omole, A. G. Radnaev, R. Rines, M. Saffman, E. Shabtai, M. H. Teo, B. Thotakura, T. Tomesh, and A. K. Tucker. Fault-tolerant operation and materials science with neutral atom logical qubits. *arXiv preprint arXiv:2412.07670*, 2024.
- [4] D. Bluvstein, S. J. Evered, A. A. Geim, S. H. Li, H. Zhou, T. Manovitz, S. Ebadi, M. Cain, M. Kalinowski, D. Hangleiter, J. P. Bonilla Ataides, N. Maskara, I. Cong, X. Gao, P. Sales Rodriguez, T. Karolyshyn, G. Semeghini, M. J. Gullans, M. Greiner, V. Vuletić, and M. D. Lukin. Logical quantum processor based on reconfigurable atom arrays. *Nature*, 626(7997):58–65, Feb. 2024.
- [5] D. Bluvstein, A. A. Geim, S. H. Li, S. J. Evered, J. Ataides, G. Baranes, A. Gu, T. Manovitz, M. Xu, M. Kalinowski, et al. Architectural mechanisms of a universal fault-tolerant quantum computer. *arXiv preprint arXiv:2506.20661*, 2025.
- [6] D. Bluvstein, H. Levine, G. Semeghini, T. T. Wang, S. Ebadi, M. Kalinowski, A. Keesling, N. Maskara, H. Pichler, M. Greiner, et al. A quantum processor based on coherent transport of entangled atom arrays. *Nature*, 604(7906):451–456, 2022.
- [7] H. Bombín. Single-shot fault-tolerant quantum error correction. *Physical Review X*, 5(3):031043, 2015.
- [8] H. Bombin. 2d quantum computation with 3d topological codes. *arXiv preprint arXiv:1810.09571*, 2018.
- [9] H. Bombin and M.-A. Martin-Delgado. Topological computation without braiding. *Physical review letters*, 98(16):160502, 2007.
- [10] H. Bombín, M. Pant, S. Roberts, and K. I. Seetharam. Fault-tolerant postselection for low-overhead magic state preparation. *PRX Quantum*, 5:010302, Jan 2024.
- [11] J. P. Bonilla Ataides, D. K. Tuckett, S. D. Bartlett, S. T. Flammia, and B. J. Brown. The xzzx surface code. *Nature Communications*, 12(1), Apr. 2021.

- [12] J. P. Bonilla Ataides, H. Zhou, Q. Xu, G. Baranes, B. Li, M. D. Lukin, and L. Jiang. Constant-overhead fault-tolerant bell-pair distillation using high-rate codes. *arXiv preprint arXiv:2502.09542*, 2025.
- [13] S. Bravyi, A. W. Cross, J. M. Gambetta, D. Maslov, P. Rall, and T. J. Yoder. High-threshold and low-overhead fault-tolerant quantum memory. *Nature*, 627(8005):778–782, 2024.
- [14] S. Bravyi and J. Haah. Magic-state distillation with low overhead. *Physical Review A—Atomic, Molecular, and Optical Physics*, 86(5):052329, 2012.
- [15] S. Bravyi and A. Kitaev. Universal quantum computation with ideal clifford gates and noisy ancillas. *Physical Review A—Atomic, Molecular, and Optical Physics*, 71(2):022316, 2005.
- [16] N. P. Breuckmann, M. Davydova, J. N. Eberhardt, and N. Tantivasadakarn. Cups and gates i: Cohomology invariants and logical quantum operations. *arXiv preprint arXiv:2410.16250*, 2024.
- [17] N. P. Breuckmann and J. N. Eberhardt. Balanced product quantum codes. *IEEE Transactions on Information Theory*, 67(10):6653–6674, 2021.
- [18] B. J. Brown, N. H. Nickerson, and D. E. Browne. Fault-tolerant error correction with the gauge color code. *Nature Communications*, 7(1), July 2016.
- [19] A. R. Calderbank and P. W. Shor. Good quantum error-correcting codes exist. *Physical Review A*, 54(2):1098, 1996.
- [20] E. T. Campbell. A theory of single-shot error correction for adversarial noise. *Quantum Science and Technology*, 4(2):025006, 2019.
- [21] E. T. Campbell, H. Anwar, and D. E. Browne. Magic-state distillation in all prime dimensions using quantum reed-muller codes. *Physical Review X*, 2(4):041021, 2012.
- [22] J. Chen, Y. Yan, and Y. Zhou. Magic of quantum hypergraph states. *Quantum*, 8:1351, 2024.
- [23] N.-C. Chiu, E. C. Trapp, J. Guo, M. H. Abobeih, L. M. Stewart, S. Hollerith, P. Stroganov, M. Kalinowski, A. A. Geim, S. J. Evered, S. H. Li, L. M. Peters, D. Bluvstein, T. T. Wang, M. Greiner, V. Vuletić, and M. D. Lukin. Continuous operation of a coherent 3,000-qubit system. *arXiv preprint arXiv:2506.20660*, 2025.
- [24] M. Christandl, F. Geshmundo, and J. Zuidam. A gap in the subrank of tensors. *SIAM Journal on Applied Algebra and Geometry*, 7(4):742–767, 2023.
- [25] L. Z. Cohen, I. H. Kim, S. D. Bartlett, and B. J. Brown. Low-overhead fault-tolerant quantum computing using long-range connectivity. *Science Advances*, 8(20), 2022.
- [26] A. Cross, Z. He, P. Rall, and T. Yoder. Improved QLDPC Surgery: Logical Measurements and Bridging Codes. *arXiv preprint arXiv:2407.18393*, 2024.
- [27] A. Cross, Z. He, P. Rall, and T. Yoder. Linear-Size Ancilla Systems for Logical Measurements in QLDPC Codes. *arXiv preprint arXiv:2407.18393*, 2024.

[28] L. Daguerre, R. Blume-Kohout, N. C. Brown, D. Hayes, and I. H. Kim. Experimental demonstration of high-fidelity logical magic states from code switching. *arXiv preprint arXiv:2506.14169*, 2025.

[29] B. Eastin and E. Knill. Restrictions on transversal encoded quantum gate sets. *Physical review letters*, 102(11):110502, 2009.

[30] J. N. Eberhardt and V. Steffan. Logical operators and fold-transversal gates of bivariate bicycle codes. *IEEE Transactions on Information Theory*, 2024.

[31] S. J. Evered, D. Bluvstein, M. Kalinowski, S. Ebadi, T. Manovitz, H. Zhou, S. H. Li, A. A. Geim, T. T. Wang, N. Maskara, et al. High-fidelity parallel entangling gates on a neutral-atom quantum computer. *Nature*, 622(7982):268–272, 2023.

[32] C. Gidney. Stim: a fast stabilizer circuit simulator. *Quantum*, 5:497, 2021.

[33] C. Gidney. How to factor 2048 bit rsa integers with less than a million noisy qubits. *arXiv preprint arXiv:2505.15917*, 2025.

[34] C. Gidney, M. Newman, P. Brooks, and C. Jones. Yoked surface codes, 2023.

[35] L. Golowich and T.-C. Lin. Quantum ldpc codes with transversal non-clifford gates via products of algebraic codes. *arXiv preprint arXiv:2410.14662*, 2024.

[36] D. Gottesman. Theory of fault-tolerant quantum computation. *Physical Review A*, 57(1):127, 1998.

[37] D. Gottesman and I. L. Chuang. Demonstrating the viability of universal quantum computation using teleportation and single-qubit operations. *Nature*, 402(6760):390–393, 1999.

[38] Gurobi Optimization, LLC. Gurobi Optimizer Reference Manual, 2024.

[39] F. Gyger, M. Ammenwerth, R. Tao, H. Timme, S. Snigirev, I. Bloch, and J. Zeiher. Continuous operation of large-scale atom arrays in optical lattices. *Phys. Rev. Res.*, 6:033104, Jul 2024.

[40] M. B. Hastings and J. Haah. Distillation with sublogarithmic overhead. *Physical review letters*, 120(5):050504, 2018.

[41] A. Hatcher. *Algebraic topology*. Cambridge University Press, Cambridge, 2002.

[42] S. Heußen and J. Hilder. Efficient fault-tolerant code switching via one-way transversal cnot gates. *arXiv preprint arXiv:2409.13465*, 2024.

[43] Y. Hong. Single-shot preparation of hypergraph product codes via dimension jump. *arXiv preprint arXiv:2410.05171*, 2024.

[44] W. C. Huffman, J.-L. Kim, and P. Solé. *Concise encyclopedia of coding theory*. Chapman and Hall/CRC, 2021.

[45] B. Ide, M. G. Gowda, P. J. Nadkarni, and G. Dauphinais. Fault-tolerant logical measurements via homological measurement. *arXiv preprint arXiv:2410.02753*, 2024.

[46] A. Ignatiev, A. Morgado, and J. Marques-Silva. PySAT: A Python toolkit for prototyping with SAT oracles. In *SAT*, pages 428–437, 2018.

[47] A. Jacob, C. McLauchlan, and D. E. Browne. Single-shot decoding and fault-tolerant gates with trivariate tricycle codes. *arXiv preprint arXiv:2508.08191*, 2025.

[48] S. Kopparty, G. Moshkovitz, and J. Zuiddam. Geometric rank of tensors and subrank of matrix multiplication. *arXiv preprint arXiv:2002.09472*, 2020.

[49] A. A. Kovalev and L. P. Pryadko. Quantum kronecker sum-product low-density parity-check codes with finite rate. *Physical Review A—Atomic, Molecular, and Optical Physics*, 88(1):012311, 2013.

[50] A. Krishna and J.-P. Tillich. Towards low overhead magic state distillation. *Physical review letters*, 123(7):070507, 2019.

[51] A. J. Landahl, J. T. Anderson, and P. R. Rice. Fault-tolerant quantum computing with color codes. *arXiv preprint arXiv:1108.5738*, 2011.

[52] J. S. Leon. A probabilistic algorithm for computing minimum weights of large error-correcting codes. *IEEE Transactions on Information Theory*, 34(5):1354–1359, 1988.

[53] A. Leverrier and G. Zémor. Quantum tanner codes. In *2022 IEEE 63rd Annual Symposium on Foundations of Computer Science (FOCS)*, pages 872–883. IEEE, 2022.

[54] H.-K. Lin and L. P. Pryadko. Quantum two-block group algebra codes. *Physical Review A*, 109(2):022407, 2024.

[55] T.-C. Lin. Transversal non-clifford gates for quantum ldpc codes on sheaves. *arXiv preprint arXiv:2410.14631*, 2024.

[56] W.-H. Lin, D. B. Tan, and J. Cong. Reuse-aware compilation for zoned quantum architectures based on neutral atoms. In *2025 IEEE International Symposium on High Performance Computer Architecture (HPCA)*, pages 127–142. IEEE, 2025.

[57] S. Loor. From möbius strips to twisted toric codes.

[58] S. Ma, G. Liu, P. Peng, B. Zhang, S. Jandura, J. Claes, A. P. Burgers, G. Pupillo, S. Puri, and J. D. Thompson. High-fidelity gates and mid-circuit erasure conversion in an atomic qubit. *Nature*, 622(7982):279–284, 2023.

[59] N. Maskara, Q. Xu, and et al. Batched high-rate logical operations for quantum ldpc codes. *To be published*, 2025.

[60] R. Mehta, J. P. Bonilla Ataides, G. Baranes, M. Cain, H. Zhou, L. Jiang, and M. D. Lukin. Dynamically generated logical gates. In preparation.

[61] S. A. Moses, C. H. Baldwin, M. S. Allman, R. Ancona, L. Ascarrunz, C. Barnes, J. Bartolotta, B. Bjork, P. Blanchard, M. Bohn, J. G. Bohnet, N. C. Brown, N. Q. Burdick, W. C. Burton, S. L. Campbell, J. P. Campora, C. Carron, J. Chambers, J. W. Chan, Y. H. Chen, A. Chernoguzov, E. Chertkov, J. Colina, J. P. Curtis, R. Daniel, M. DeCross, D. Deen,

C. Delaney, J. M. Dreiling, C. T. Ertsgaard, J. Esposito, B. Estey, M. Fabrikant, C. Figgatt, C. Foltz, M. Foss-Feig, D. Francois, J. P. Gaebler, T. M. Gatterman, C. N. Gilbreth, J. Giles, E. Glynn, A. Hall, A. M. Hankin, A. Hansen, D. Hayes, B. Higashi, I. M. Hoffman, B. Horning, J. J. Hout, R. Jacobs, J. Johansen, L. Jones, J. Karcz, T. Klein, P. Lauria, P. Lee, D. Liefer, S. T. Lu, D. Lucchetti, C. Lytle, A. Malm, M. Matheny, B. Mathewson, K. Mayer, D. B. Miller, M. Mills, B. Neyenhuis, L. Nugent, S. Olson, J. Parks, G. N. Price, Z. Price, M. Pugh, A. Ransford, A. P. Reed, C. Roman, M. Rowe, C. Ryan-Anderson, S. Sanders, J. Sedlacek, P. Shevchuk, P. Siegfried, T. Skripka, B. Spaun, R. T. Sprenkle, R. P. Stutz, M. Swallows, R. I. Tobey, A. Tran, T. Tran, E. Vogt, C. Volin, J. Walker, A. M. Zolot, and J. M. Pino. A race-track trapped-ion quantum processor. *Phys. Rev. X*, 13:041052, Dec 2023.

[62] D. E. Muller. Application of boolean algebra to switching circuit design and to error detection. *Transactions of the IRE professional group on electronic computers*, (3):6–12, 1954.

[63] Q. T. Nguyen. Good binary quantum codes with transversal ccz gate. doi: 10.48550. *arXiv preprint arXiv:2408.10140*, 2024.

[64] D. Nigg, M. Mueller, E. A. Martinez, P. Schindler, M. Hennrich, T. Monz, M. A. Martin-Delgado, and R. Blatt. Quantum computations on a topologically encoded qubit. *Science*, 345(6194):302–305, 2014.

[65] P. Pantaleev and G. Kalachev. Degenerate quantum ldpc codes with good finite length performance. *Quantum*, 5:585, 2021.

[66] P. Pantaleev and G. Kalachev. Quantum ldpc codes with almost linear minimum distance. *IEEE Transactions on Information Theory*, 68(1):213–229, 2021.

[67] P. Pantaleev and G. Kalachev. Asymptotically good quantum and locally testable classical ldpc codes. In *Proceedings of the 54th annual ACM SIGACT symposium on theory of computing*, pages 375–388, 2022.

[68] L. P. Pryadko, V. A. Shabashov, and V. K. Kozin. Qdistrnd: A gap package for computing the distance of quantum error-correcting codes. *arXiv preprint arXiv:2308.15140*, 2023.

[69] I. S. Reed. A class of multiple-error-correcting codes and the decoding scheme. Technical report, 1953.

[70] B. W. Reichardt, A. Paetznick, D. Aasen, I. Basov, J. M. Bello-Rivas, P. Bonderson, R. Chao, W. van Dam, M. B. Hastings, R. V. Mishmash, A. Paz, M. P. da Silva, A. Sundaram, K. M. Svore, A. Vaschillo, Z. Wang, M. Zanner, W. B. Cairncross, C.-A. Chen, D. Crow, H. Kim, J. M. Kindem, J. King, M. McDonald, M. A. Norcia, A. Ryou, M. Stone, L. Wadleigh, K. Barnes, P. Battaglino, T. C. Bohdanowicz, G. Booth, A. Brown, M. O. Brown, K. Cassella, R. Coxe, J. M. Epstein, M. Feldkamp, C. Griger, E. Halperin, A. Heinz, F. Hummel, M. Jaffe, A. M. W. Jones, E. Kapit, K. Kotru, J. Lauigan, M. Li, J. Marjanovic, E. Megidish, M. Meredith, R. Morshead, J. A. Muniz, S. Narayanaswami, C. Nishiguchi, T. Paule, K. A. Pawlak, K. L. Pudenz, D. R. Pérez, J. Simon, A. Smull, D. Stack, M. Urbanek, R. J. M. van de Veerdonk, Z. Vendeiro, R. T. Weverka, T. Wilkason, T.-Y. Wu, X. Xie, E. Zalys-Geller, X. Zhang, and B. J. Bloom. Fault-tolerant quantum computation with a neutral atom processor. *arXiv preprint arXiv:2411.11822*, 2025.

- [71] J. Roffe. LDPC: Python tools for low density parity check codes, 2022.
- [72] J. Roffe, D. R. White, S. Burton, and E. Campbell. Decoding across the quantum low-density parity-check code landscape. *Phys. Rev. Res.*, 2:043423, Dec 2020.
- [73] P. Sales Rodriguez, J. M. Robinson, P. N. Jepsen, Z. He, C. Duckering, C. Zhao, K.-H. Wu, J. Campo, K. Bagnall, M. Kwon, et al. Experimental demonstration of logical magic state distillation. *Nature*, pages 1–3, 2025.
- [74] P. Scholl, M. Schuler, H. J. Williams, A. A. Eberharter, D. Barredo, K.-N. Schymik, V. Lienhard, L.-P. Henry, T. C. Lang, T. Lahaye, et al. Quantum simulation of 2d antiferromagnets with hundreds of rydberg atoms. *Nature*, 595(7866):233–238, 2021.
- [75] T. R. Scruby, D. E. Browne, P. Webster, and M. Vasmer. Numerical Implementation of Just-In-Time Decoding in Novel Lattice Slices Through the Three-Dimensional Surface Code. *Quantum*, 6:721, May 2022.
- [76] T. R. Scruby, K. Nemoto, and Z. Cai. Fault-tolerant quantum computation without distillation on a 2d device, 2025.
- [77] T. R. Scruby, A. Pesah, and M. Webster. Quantum rainbow codes. *arXiv preprint arXiv:2408.13130*, 2024.
- [78] P. W. Shor. Algorithms for quantum computation: discrete logarithms and factoring. In *Proceedings 35th annual symposium on foundations of computer science*, pages 124–134. Ieee, 1994.
- [79] M. D. Shulman, O. E. Dial, S. P. Harvey, H. Bluhm, V. Umansky, and A. Yacoby. Demonstration of entanglement of electrostatically coupled singlet-triplet qubits. *science*, 336(6078):202–205, 2012.
- [80] M. Sipser and D. A. Spielman. Expander codes. *IEEE transactions on Information Theory*, 42(6):1710–1722, 2002.
- [81] Y. Stade, W.-H. Lin, J. Cong, and R. Wille. Routing-aware placement for zoned neutral atom-based quantum computing. *arXiv preprint arXiv:2505.22715*, 2025.
- [82] Y. Stade, L. Schmid, L. Burgholzer, and R. Wille. Optimal state preparation for logical arrays on zoned neutral atom quantum computers. In *2025 Design, Automation and Test in Europe Conference (DATE)*, pages 1–7, 2025.
- [83] A. Steane. Multiple-particle interference and quantum error correction. *Proceedings of the Royal Society of London. Series A: Mathematical, Physical and Engineering Sciences*, 452(1954):2551–2577, 1996.
- [84] M. Sullivan. Code conversion with the quantum golay code for a universal transversal gate set. *Physical Review A*, 109(4):042416, 2024.
- [85] E. Swaroop, T. Jochym-O'Connor, and T. J. Yoder. Universal adapters between quantum ldpc codes, 2024.

[86] B. Tan, D. Bluvstein, M. D. Lukin, and J. Cong. Qubit mapping for reconfigurable atom arrays. In *Proceedings of the 41st IEEE/ACM International Conference on Computer-Aided Design*, pages 1–9, 2022.

[87] D. B. Tan, D. Bluvstein, M. D. Lukin, and J. Cong. Compiling quantum circuits for dynamically field-programmable neutral atoms array processors. *Quantum*, 8:1281, 2024.

[88] D. B. Tan, W.-H. Lin, and J. Cong. Compilation for dynamically field-programmable qubit arrays with efficient and provably near-optimal scheduling. In *Proceedings of the 30th Asia and South Pacific Design Automation Conference*, pages 921–929, 2025.

[89] D. B. Tan, S. Ping, and J. Cong. Depth-optimal addressing of 2D qubit array with 1D controls based on exact binary matrix factorization. In *2024 Design, Automation and Test in Europe Conference and Exhibition (DATE) Proceedings*, 2024.

[90] J.-P. Tillich and G. Zémor. Quantum ldpc codes with positive rate and minimum distance proportional to the square root of the blocklength. *IEEE Transactions on Information Theory*, 60(2):1193–1202, 2013.

[91] J. Viszlai, W. Yang, S. F. Lin, J. Liu, N. Nottingham, J. M. Baker, and F. T. Chong. Matching generalized-bicycle codes to neutral atoms for low-overhead fault-tolerance. *arXiv preprint arXiv:2311.16980*, 2024.

[92] K. Wang, Z. Lu, C. Zhang, G. Liu, J. Chen, Y. Wang, Y. Wu, S. Xu, X. Zhu, F. Jin, Y. Gao, Z. Tan, Z. Cui, N. Wang, Y. Zou, A. Zhang, T. Li, F. Shen, J. Zhong, Z. Bao, Z. Zhu, Y. Han, Y. He, J. Shen, H. Wang, J.-N. Yang, Z. Song, J. Deng, H. Dong, Z.-Z. Sun, W. Li, Q. Ye, S. Jiang, Y. Ma, P.-X. Shen, P. Zhang, H. Li, Q. Guo, Z. Wang, C. Song, H. Wang, and D.-L. Deng. Demonstration of low-overhead quantum error correction codes. *arXiv preprint arXiv:2505.09684*, 2025.

[93] D. J. Williamson and T. J. Yoder. Low-overhead fault-tolerant quantum computation by gauging logical operators. *arXiv preprint arXiv:2410.02213*, 2024.

[94] A. Wills, M.-H. Hsieh, and H. Yamasaki. Constant-overhead magic state distillation. *arXiv preprint arXiv:2408.07764*, 2024.

[95] Q. Xu, J. P. Bonilla Ataides, C. A. Pattison, N. Raveendran, D. Bluvstein, J. Wurtz, B. Vasić, M. D. Lukin, L. Jiang, and H. Zhou. Constant-overhead fault-tolerant quantum computation with reconfigurable atom arrays. *Nature Physics*, 20(7):1084–1090, 2024.

[96] Q. Xu, H. Zhou, G. Zheng, D. Bluvstein, J. P. B. Ataides, M. D. Lukin, and L. Jiang. Fast and parallelizable logical computation with homological product codes. *Physical Review X*, 15(2):021065, 2025.

[97] T. J. Yoder, E. Schoute, P. Rall, E. Pritchett, J. M. Gambetta, A. W. Cross, M. Carroll, and M. E. Beverland. Tour de gross: A modular quantum computer based on bivariate bicycle codes. *arXiv preprint arXiv:2506.03094*, 2025.

[98] W. Zeng and L. P. Pryadko. Higher-dimensional quantum hypergraph-product codes with finite rates. *Physical review letters*, 122(23):230501, 2019.

- [99] H. Zhou, C. Duckering, C. Zhao, D. Bluvstein, M. Cain, A. Kubica, S.-T. Wang, and M. D. Lukin. Resource analysis of low-overhead transversal architectures for reconfigurable atom arrays. In *Proceedings of the 52nd Annual International Symposium on Computer Architecture*, pages 1432–1448, 2025.
- [100] G. Zhu. A topological theory for qldpc: non-clifford gates and magic state fountain on homological product codes with constant rate and beyond the $n^{1/3}$ distance barrier. *arXiv preprint arXiv:2501.19375*, 2025.
- [101] G. Zhu. Transversal non-clifford gates on qldpc codes breaking the \sqrt{N} distance barrier and quantum-inspired geometry with \mathbb{Z}_2 systolic freedom. *arXiv preprint arXiv:2507.15056*, 2025.

Supplemental Material

Review of homological formulation of CSS Codes

Background on cohomology

A *cochain complex* (C^\bullet, d^\bullet) is a sequence of vector spaces over a field, or more generally modules over a ring, equipped with linear maps

$$\dots \xrightarrow{d^{i-2}} C^{i-1} \xrightarrow{d^{i-1}} C^i \xrightarrow{d^i} C^{i+1} \xrightarrow{d^{i+1}} \dots$$

such that

$$d^i \circ d^{i-1} = 0 \quad \text{for all } i. \quad (44)$$

This condition ensures that the image of one map is always contained in the kernel of the next:

$$\text{im}(d^{i-1}) \subseteq \ker(d^i). \quad (45)$$

Elements of C^i are called *i-cochains*. Elements of $\ker(d^i) \subseteq C^i$ are called *i-cocycles*, and elements of $\text{im}(d^{i-1}) \subseteq C^i$ are called *i-coboundaries*. Since every coboundary is automatically a cocycle, we may define the *i-th cohomology group* (or space) as the space of cocycles modulo coboundaries:

$$H^i(C^\bullet) := \ker(d^i) / \text{im}(d^{i-1}). \quad (46)$$

Cohomology detects elements in C^i that are annihilated by d^i but are not exact—i.e., not the image of any element under d^{i-1} .

For context, the dual notion is that of a *chain complex*, where the maps go in the opposite direction. The homology of a chain complex is defined analogously, with

$$H_i(C_\bullet) := \ker(\partial_i) / \text{im}(\partial_{i+1}),$$

When the C^i are finite-dimensional vector spaces or free modules (modules that admit a basis), there is a natural identification $C_i \cong (C^i)^*$, and the differentials satisfy $d^i = (\partial_{i+1})^T$. In this case, there is a canonical isomorphism between homology and cohomology:

$$H^i(C^\bullet) \cong H_i(C_\bullet). \quad (47)$$

This identification is particularly useful when interpreting CSS codes and their logical operators in terms of cohomology.

Classical codes from cochain complexes

A classical binary linear code $C \subset \mathbb{F}_2^n$ is a k -dimensional subspace with minimum distance $d = \min_{c \in C} |c|$, where $|\cdot|$ denotes the Hamming weight. The code is specified by a parity check matrix $H \in \mathbb{F}_2^{n \times r}$ such that $\ker(H) = C$.

This data can be represented as a 2-term cochain complex:

$$C^\bullet : \quad \mathbb{F}_2^r \xrightarrow{H^T} \mathbb{F}_2^n \quad (48)$$

where \mathbb{F}_2^n (in degree 1) represents the bits and \mathbb{F}_2^r (in degree 0) the checks. The map H^T is the coboundary operator, and the codewords are given by the degree-1 cohomology: $H^1(C^\bullet) = \ker(H) = \text{coker}(H^T)$.

A choice of basis for \mathbb{F}_2^r and \mathbb{F}_2^n corresponds to choosing generators for the checks and a coordinate system for the message space. Code parameters will be denoted by $[n, k, d]$.

Quantum CSS codes as 3-term cochain complexes

A quantum CSS code is defined by a pair of classical binary codes $C_X, C_Z \subseteq \mathbb{F}_2^n$ satisfying the inclusion $C_Z^\perp \subseteq C_X$, which is equivalent to $H_X H_Z^T = 0$. This ensures commutativity of the corresponding stabilizer operators.

This data defines a 3-term cochain complex:

$$C^\bullet : \quad \mathbb{F}_2^{r_Z} \xrightarrow{H_Z^T} \mathbb{F}_2^n \xrightarrow{H_X} \mathbb{F}_2^{r_X} \quad (49)$$

where \mathbb{F}_2^n (degree 1) represents the qubits, H_Z^T defines the Z -type stabilizers, and H_X defines the X -type stabilizers. The degree-1 cohomology $H^1(C^\bullet) = \ker(H_X)/\text{im}(H_Z^T)$ defines the Z -logical operators, while the degree-1 homology $H_1(C_\bullet) = \ker(H_Z)/\text{im}(H_X^T)$ defines the X -logical operators. The number of encoded qubits is

$$k = \dim H^1(C^\bullet) = \dim H_1(C_\bullet),$$

and the distance is $d = \min(d_X, d_Z)$, where d_X and d_Z are the minimum weights of nontrivial logical X and Z operators, respectively.

More generally, any n -term (co)chain complex with $n \geq 3$ can define a CSS code by selecting three consecutive terms $C^{i-1} \rightarrow C^i \rightarrow C^{i+1}$.

Homological products

We describe two constructions for combining classical codes to produce quantum codes: the tensor product and the balanced product. The tensor product generalizes the hypergraph product. The balanced product incorporates group symmetries to reduce size while preserving code properties.

Tensor products of cochain complexes

Let (C^\bullet, δ^C) and (D^\bullet, δ^D) be cochain complexes of \mathbb{F}_2 -vector spaces. Their tensor product is a new cochain complex defined by

$$(C \otimes D)^n = \bigoplus_{i+j=n} C^i \otimes D^j, \quad (50)$$

with coboundary operator

$$\delta(c \otimes d) = \delta^C(c) \otimes d + (-1)^i c \otimes \delta^D(d), \quad \text{for } c \in C^i, d \in D^j. \quad (51)$$

When working over \mathbb{F}_2 , the sign $(-1)^i$ may be omitted.

Tensoring an m -term and an n -term cochain complex yields an $(m + n - 1)$ -term complex. This construction applies directly to the cochain complexes associated with classical codes. The hypergraph product of two classical codes is the CSS code associated with the 3-term tensor product of their respective 2-term cochain complexes. In Section 4.3, we show how the Künneth formula recovers the standard dimension and distance bounds for hypergraph product codes.

Balanced products

The balanced product modifies the tensor product by incorporating a group symmetry. This typically reduces the code size while preserving—or sometimes improving—the relative distance and rate.

Balanced Product of Vector Spaces

Let V and W be \mathbb{F}_2 -vector spaces equipped with compatible linear G -actions. Then V and W are modules over the group algebra $\mathbb{F}_2[G]$. The *balanced product* is defined as

$$V \otimes_G W := V \otimes_{\mathbb{F}_2[G]} W. \quad (52)$$

This is the quotient of the standard tensor product by the subspace generated by elements of the form

$$g \cdot v \otimes w - v \otimes g \cdot w, \quad \text{for all } g \in G, v \in V, w \in W. \quad (53)$$

In terms of bases, let X and Y be G -invariant bases for V and W . Then a basis for $V \otimes_G W$ is given by the orbits of the anti-diagonal group action:

$$X \times_G Y := X \times Y / \{(g^{-1}x, gy) : g \in G\}. \quad (54)$$

Balanced Product of Cochain Complexes

Let G be a finite (Abelian) group, and let C^\bullet, D^\bullet be cochain complexes of \mathbb{F}_2 -vector spaces equipped with a linear G -action on each term. Assume the coboundary maps δ^C, δ^D commute with the group action:

$$g \cdot \delta^C(x) = \delta^C(g \cdot x), \quad g \cdot \delta^D(y) = \delta^D(g \cdot y). \quad (55)$$

The balanced product complex is defined by

$$(C \otimes_G D)^n = \bigoplus_{i+j=n} C^i \otimes_G D^j, \quad (56)$$

with coboundary operator

$$\delta = \delta^C \otimes \mathbb{I} + \mathbb{I} \otimes \delta^D. \quad (57)$$

This defines a valid cochain complex. As with the tensor product, quantum CSS codes can be constructed by selecting three consecutive terms of the balanced product complex.

We will particularly be interested in the case where C and D are complexes where the cochain spaces are direct sums of $\mathbb{F}_2[G]$ itself, as this is the scenario defining group-algebra quantum codes.

In this case, the bases for the cochain spaces are given by copies of G . For example, we may consider then consider the balanced product of two 2-term co-chain complexes

$$\mathbb{F}_2[G] \xrightarrow{a} \mathbb{F}_2[G] \quad \mathbb{F}_2[G] \xrightarrow{b} \mathbb{F}_2[G]$$

where the coboundary maps are respectively defined by algebra multiplication by $a \in \mathbb{F}_2[G]$ and $b \in \mathbb{F}_2[G]$. Using the notation $R \equiv \mathbb{F}_2[G]$, the balanced product complex is given by

$$R \otimes_R R \xrightarrow{\begin{pmatrix} a \otimes \text{id} \\ \text{id} \otimes b \end{pmatrix}} R \otimes_R R \oplus R \otimes_R R \xrightarrow{\begin{pmatrix} \text{id} \otimes b & a \otimes \text{id} \end{pmatrix}} R \otimes_R R \quad (58)$$

For module tensor products of R with itself, we have a useful isomorphism $R \otimes_R R \cong R$ given by $r \otimes_R s \cong rs$ (see Appendix A of [30] for example). This yields the bicycle code chain complex in Eq. (17). Iterating the balanced product with a third classical complex defined by $c \in \mathbb{F}_2[G]$ yields the complex in Eq. (18).

Künneth Theorem

The Künneth theorem provides a formula for computing the cohomology of a tensor product of cochain complexes from the cohomologies of the constituent complexes.

Let C^\bullet and D^\bullet be cochain complexes of vector spaces over a field, such as \mathbb{F}_2 . Then the Künneth theorem states:

$$H^n(C^\bullet \otimes D^\bullet) \cong \bigoplus_{i+j=n} H^i(C^\bullet) \otimes H^j(D^\bullet). \quad (59)$$

This expression holds exactly when working over a field and allows one to compute the cohomology of the product complex from the cohomologies of the factors.

More generally, suppose C^\bullet and D^\bullet are cochain complexes of modules over a finite-dimensional algebra A over a field, such as $\mathbb{F}_2[G]$ for a finite group G . Then the Künneth formula similarly holds [57]:

$$H^n(C^\bullet \otimes_A D^\bullet) \cong \bigoplus_{i+j=n} H^i(C^\bullet) \otimes_A H^j(D^\bullet), \quad (60)$$

where \otimes_A denotes the tensor product over the algebra A – i.e the balanced product.